The Effect of Directional Wind Shear and Evolving Synoptic-Scale Flow on Vortex Shedding

Lucas Michael Harris

A thesis submitted in partial fulfillment of the requirements for the degree of

Master of Science

University of Washington

2006

Program Authorized to Offer Degree: Atmospheric Sciences

University of Washington
Graduate School

This is to certify that I have examined this copy of a master's thesis by

Lucas Michael Harris

and have found that it is complete and satisfactory in all respects,
and that any and all revisions required by the final
examining committee have been made.

Committee Members:

_____
Dale R. Durran

_____
Gregory J. Hakim

_____
Christopher S. Bretherton

Date: _____

In presenting this thesis in partial fulfillment of the requirements for a master's degree at the University of Washington, I agree that the Library shall make its copies freely available for inspection. I further agree that extensive copying of this thesis is allowable only for scholarly purposes, consistent with "fair use" as prescribed in the U.S. Copyright Law. Any other reproduction for any purpose or by any means shall not be allowed without my written permission.

Signature_____

Date_____

TABLE OF CONTENTS

LIST OF FIGURES

LIST OF TABLES

Chapter 1

INTRODUCTION

The observation of atmospheric vortices in the lees of isolated oceanic mountains in early satellite images led to the creation of a body of research to determine the cause of this remarkable phenomenon. Notable for their beauty (Figure 1.1) and seeming improbability, atmospheric lee vortices have had a number of different theories postulated, expounded, and sometimes rejected over the past four decades regarding the mechanism of their formation and the atmospheric conditions in which they are most likely to appear.

Lee vortices were identified in images sent from early TIROS (Television Infrared Observation Satellite) instruments as early as 1962 (Hubert and Krueger, 1962) and was immediately followed by discussion on how these vortices were formed. Several ideas were proposed over the following two decades, including that the vortices were the manifestation of an inertial instability or were the result of a traveling trapped wave (Chopra and Hubert, 1965).

The consensus explanation (Brighton, 1978) for some time (and still given today in some popular accounts) was that the vortices were analogous to the familiar von Karman vortex streets (Kundu and Cohen, 2002, ch. 10) in laboratory flows. These vortices form through the generation of a viscous boundary layer on the surface of a steep-sided object, such as a cylinder, building, or insect wing in a homogeneous viscous fluid at certain values of the Reynolds number. The shear generated in this boundary layer produces vorticity aligned parallel to the principal axis of the obstacle, which then becomes shed vortices when the boundary layer separates from the object.

Figure 1.1: Lee vortices off of the Cape Verde Islands on 5 January 2005, as imaged by the MODIS instrument on the NASA Terra satellite.

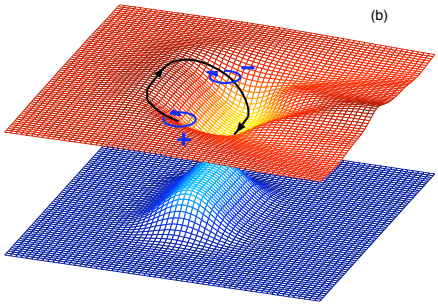

Figure 1.2: Schematic of the SR89 vorticity production mechanism, showing a mountain ridge with an isentropic surface (red) and a tilted vortex line (black), depicting the generation of vertical vorticity (ζ). From Epifanio (2003).

The viscous hypothesis was rejected after the results of the inviscid, free-slip simulations of Smolarkiewicz and Rotunno (1989, henceforth SR89). These simulations used an infinitely deep, continuously and stably stratified flow past a sloped mountain, rather than the earlier approach of homogeneous flow past steep-sided obstacles. Despite no processes in which a viscous boundary layer could form, vorticity was still being produced and vortices appeared in the mountain's wake. They concluded that some inviscid process must be creating vorticity, and since the only term in the inviscid vorticity equation which is nonzero in an initally irrotational flow is the baroclinic term, which only produces horizontal vorticity, then the vortices must originate through the creation of vorticity through buoyancy gradients and subsequent tilting of the resulting horizontal vorticity into the vertical. A schematic of the tilting process can be seen in Figure 1.2. It is instructive to note that this baroclinic generation mechanism is very similar to the production of rotation in supercell thunderstorms, in which the topography is replaced by the rear flank gust front and a strong updraft replaces the descent in the lee. It should also be noted that later research (Grubisić et al., 1995) found that the presence of surface friction in fact weakened the vortices, and could stabilize the wake and prevent shedding if enough friction was present.

Further development of the SR89 mechanism (Smith, 1989b; Schär and Durran, 1997; Epifanio and Durran, 2002a,b, henceforth collectively ED02) has applied the Continuous Stratification and Constant Wind model (Reinecke and Durran, 2006), typically used for predicting the appearance of wave breaking, to determine under which conditions lee vortex formation is most likely. This theory is cast in terms of the nonlinearity parameter $\varepsilon = \frac{NH}{U}$, for a uniform upstream buoyancy frequency N and wind speed U along with the mountain height H. This parameter is then used along with the aspect ratio of the mountain (the ratio of cross-wind length to along-wind length) to determine whether or not shedding is likely, as first put forth in a diagram from Smith (1989b). In general, higher values of ε correspond to a more nonlinear flow which is more likely to cause vortex shedding.

The SR89 mechanism immediately came under criticism from several other researchers (Smith, 1989a). In particular the fact that the theory that led to this mechanism was performed with a weakly nonlinear analysis was a point of contention, with the claim that the small amplitude vorticity generation process could not generate enough vorticity to capture the magnitude of observed vortices. Another major point of contention was that the inviscid SR89 mechanism cannot create potential vorticity. An alternative hypothesis was presented in which a substantial amount of the vorticity was produced by dissipative processes in the wake, such as wave breaking and in hydraulic jumps, which cause the production of potential vorticity which in turn composed the lee vortices. ED02 found that in a continuously stratified atmosphere, the baroclinic process was the dominant process for generating vorticity, with stretching and dissipative processes being less important. However, since these vortices are strong centers of potential vorticity, either dissipative or diabatic processes must be present.

A notable feature of all of these explanations for the appearance of lee vortices is that none of them directly address the act of vortex shedding, that is, the breakup of the wake into individual vortices which then move downstream. The analytic solutions of SR89 and the symmetric simulations of Schär and Smith (1993), SD97, ED02, and others all show vortices that remain attached to the mountain and slowly grow downstream, but never start shedding. The nature of the instability needed to break up the wake was thoroughly investigated by Schär and Smith (1993, henceforth SS93b), who found that an imposed unstable mode was needed to introduce a barotropic instability in the wake and thus begin vortex shedding by disrupting the wake and allowing the vortices to break off and move downstream. Most other research on idealized vortex shedding instead impose some sort of cross-centerline asymmetry to create the instability. SD97 starts vortex shedding through the placement of a warm bubble in the lee of the mountain just off of the center line so the potential temperature field is initially asymmetric. Other researchers, such as Sun

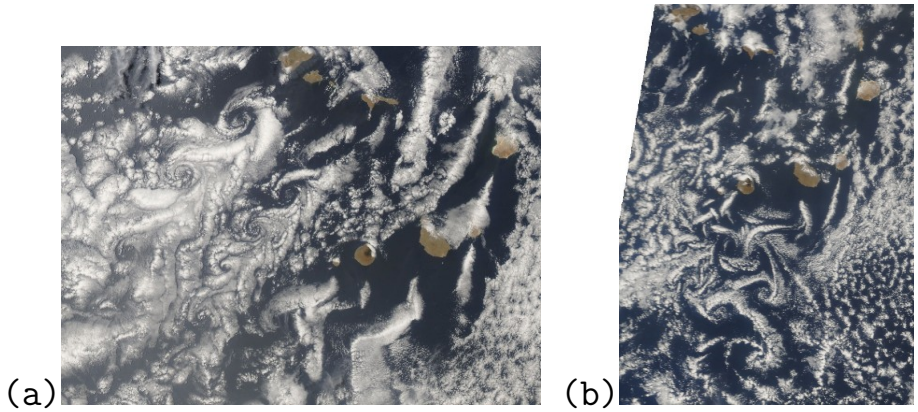

Figure 1.3: Examples of vortex shedding at the Cape Verde Islands. (a) 2 June 2005 image depicting cyclonic vortex shedding. (b) 6 June 2005 image depicting anticyclonic vortex shedding.

and Chern (1994) have imposed a Coriolis force or used asymmetric topography to start vortex shedding.

Occasionally, as in Figure 1.3, vortex shedding is seen with one sign of vortex dominating the other. Two examples from the Cape Verde Islands are presented here. In Figure 1.3a, the vortex street is clearly dominated by counter-clockwise or "cyclonic"[1] vortices. Note the elongation of Santa Antão, the island off of which the vortices are being shed; although such a non-round mountain might be expected to preferentially shed one sign of vortex over the other even in an unsheared flow, in this case the flow is nearly aligned with the mountain range on the island (running northeast to southwest) and this factor is minimized. Alternately, in Figure 1.3b clockwise or "anticyclonic" vortices can be seen which are somewhat larger and more well-defined than the corresponding cyclonic vortices. In this case, the island causing the shedding, Santiago, is more circularly symmetric than is Santa Antão.

The images can be compared with the upstream soundings available at these times.

[1]In this work Northern Hemisphere conventions are used with respect to "cyclonic" or "anti-cyclonic" motion (despite of the lack of Coriolis), so that counter-clockwise motions are deemed cyclonic.

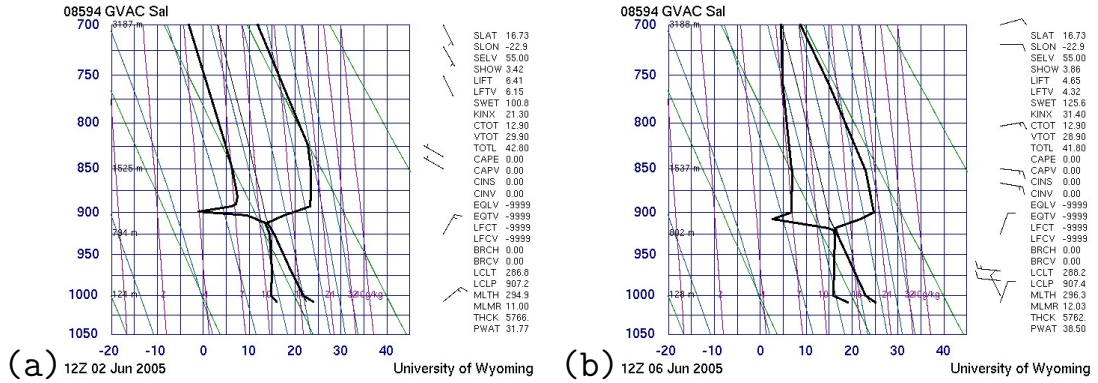

Figure 1.4: Upstream 12 UTC soundings from Sal, Cape Verde. Compare with Figure 2.2. (a) 2 June 2005 Sal sounding with cyclonic turning of the wind. (b) 6 June 2005 Sal sounding with anticyclonic turning of the wind. Note the bad easterly boundary layer wind data.

The sounding in Figure 1.4a, corresponding with the image in Figure 1.3a, shows a clear cyclonic turning of the wind with height: the flow is northeasterly near the surface and turns to the west-northwest near the top of the inversion. In Figure 1.4b, if the boundary layer westerlies (likely corresponding to some localized boundary layer eddy) are neglected, the northerlies at the surface and easterlies aloft correspond to an anticyclonic vertical shear profile. Hence, in both of these images, the vortices which dominate are those with the same sense of rotation as the turning of the wind with height.

There has been little research on the processes leading to such asymmetric vortex shedding. The research which does exist primarily addresses the role of Coriolis forces in introducing this asymmetry (Potylitsin and Peltier, 1998), whereas little attention has been given to the role of asymmetric topography or directional wind shear in the absence of Coriolis forces. Sun and Chern (1994) performed a few simulations with asymmetric topography and topography aligned at an oblique angle to the flow, but made no attempt to determine the effects on the vortices, nor did they investigate the

causes for any observed asymmetry. Sun and Chern did find that for an asymmetric mountain ridge with a higher peak on one side that the vortices tended to be larger on that higher end. Zängl (2005) looked at the effect of wind direction on the upstream response to of an elongated ridge, but did not elaborate on any downstream effects. Zangl claimed to find only one other piece of research on the effect of wind direction on an elongated ridge, a doctoral thesis by Bauer (1997).

Additionally, few studies have been performed on the impact of upstream flow unsteadiness on lee vortices or even on lee waves (Chen et al., 2005, henceforth CDH). In fact, it is sometimes assumed, as in Smith and Grønås (1993), that a slowly evolving flow can go through a series of steady states, and that such an evolving flow can be used to test a number of locations in parameter space with a single simulation, as if a given time interval could be used as a simulation of a particular steady flow.

Crook et al. (1990) performed two model runs with an imposed accelerating and decelerating mean flow. They found that in an accelerating flow no wave breaking is observed and the vortices are seen to develop from the ground up; in contrast, in a decelerating flow there is substantial wave breaking and flow reversal, indicating the formation of vortices, which begins aloft and builds down to the surface. CDH came to a similar result regarding wave breaking in unsteady flows. This finding indicates that wave breaking, even in this continuously stratified case, could have some importance in the formation of potential vorticity for the vortices.

There has been some interest in a similar situation in the oceanography and engineering literature, typically in the context of an evolving (or "oscilliatory") flow past topography or a cylinder. In particular, there has been interest in the examination of tidal flows past a seamount. Such studies include the shallow water investigations of Lloyd et al. (2001) and Stansby and Lloyd (2001), and the continuously stratified laboratory experiments of Boyer and Zhang (1990), and Zhang and Boyer (1993). However, many of these studies look at flows that evolve at least an order of magnitude faster than is observed in the atmosphere, and occur in flows with a much lower

Rossby number (U/fL, where f is the Coriolis parameter and L a characteristic length).

As seen in CDH, an evolving flow can have a profound impact on the amount of pressure drag and momentum flux produced by mountain waves. Since lee vortices have a longer advective timescale (L/U) than do mountain waves, the vortices would be expected to have an even greater dependence upon flow evolution. In particular, Doppler shifts induced by changes in flow speed could either sweep the full wake, including the vortices, downstream and away from the mountain during mean flow acceleration, or push the wake and vortices back up against and possibly around the mountain during deceleration.

The first goal of this research is to determine what environmental factors can cause asymmetric vortex shedding, and to investigate the processes which cause the preferential generation of one sign of vorticity in the lee. In particular this thesis will focus on the effects of directional wind shear on this asymmetry. Simulations suggested by observations of asymmetric vortices in a sheared flow (Figure 1.3) will be performed to reproduce the observed asymmetry, and to be able to analyze the specific process of vorticity generation to determine the fundamental dynamics leading to the asymmetry.

This study will also address the effects of an evolving flow on vortex shedding and wake behavior. The generation, structure, and behavior of lee vortices in different time-dependent flows, with differing kinematical structure, and across mountains of different heights and aspect ratios, will be examined, as will the induced pressure drag on the topography during the flow evolution.

Chapter 2
MODEL FORMULATION

Two sets of model runs were performed in this study. To study the effects of directional shear, a set of doubly-nested, finer resolution model runs were performed with a round mountain and differing initial wind profiles. A second set, using a slightly different version of the model, were performed to study flow transience using a series of flow and mountain types.

2.1 Governing Equations

The Durran and Klemp (1983) nonhydrostatic fully compressible mesoscale model was used in this study. The model uses a fully nonlinear, nonhydrostatic formulation of the governing equations discretized by a finite differencing method on an Arakawa C-grid. All simulations were performed with no surface friction or moist processes, and with a free slip surface.

The governing equations, as given in Durran and Klemp (1983) and Piani et al. (2000), are:

$$\frac{\mathrm{D}\mathbf{u}}{\mathrm{D}t} + c_p\theta\nabla(\pi+\overline{\pi}) + f\hat{\mathbf{k}}\times\mathbf{u} = g\left(\frac{\theta-\overline{\theta}}{\overline{\theta}}\right)\hat{\mathbf{k}} + \mathbf{D}$$

$$\frac{\mathrm{D}\theta}{\mathrm{D}t} = D_\theta$$

$$\frac{\mathrm{D}\left(\pi+\overline{\pi}\right)}{\mathrm{D}t} = -\frac{R}{c_v}(\overline{\pi}+\pi)\left(\nabla\cdot\mathbf{u} - \frac{1}{\theta}\frac{\mathrm{D}\theta}{\mathrm{D}t}\right)$$

where

$$\frac{\mathrm{D}}{\mathrm{D}t} = \frac{\partial}{\partial t} + (\mathbf{u}\cdot\nabla)$$

is the total derivative,

$$\pi(x,y,z,t) + \overline{\pi}(z) = \left(\frac{p}{p_0}\right)^{R/c_p}$$

is the full Exner function (perturbation plus basic state), $\hat{\mathbf{k}}$ the vertical unit vector, f the Coriolis parameter, $\mathbf{u} = (u, v, w)$ the wind velocity vector, $\theta(x, y, z, t) + \overline{\theta}(z)$ the full potential temperature, $\mathbf{D} = (D_u, D_v, D_w)$ the subgrid scale mixing of momentum (Durran and Klemp, 1983), D_θ the subgrid scale mixing of heat, c_p the specific heat at constant pressure, p the pressure, and $p_0 = 1000$ mb.

2.2 Topography

The mountains used in this study are either bell-shaped circular mountains or elongated ridges (as opposed to elliptical ridges). The mountains' heights are given by Reinecke and Durran (2006):

$$h = \begin{cases} H\left[\frac{1+\cos(\pi r)}{2}\right]^4 & \text{if } r \leq 4a \\ 0 & \text{otherwise} \end{cases} \tag{2.1}$$

where

$$r^2 = \begin{cases} \frac{|x-x_0|}{4a}^2 + (\frac{|y-y_0|-(\beta-1)a}{4a})^2 & \textbf{if } |y-y_0| > (\beta-1)a \\ \frac{|x-x_0|}{4a}^2 & \text{otherwise} \end{cases} \tag{2.2}$$

and (x_0, y_0) are the coordinates of the mountain peak, H is the height of the peak, a the half-width, and β the aspect ratio. If $\beta = 1$ the mountain is round and the expression for r^2 is simplified.

2.3 Directional Shear Runs

The directional shear model runs were performed with an outer 3 km horizontal resolution grid and an inner 1 km horizontal resolution grid. The outer grid's horizontal dimensions are 624 km by 321 km, while the inner grid is 312 km by 160.5 km. For stability, the outer grid used a 6 s large timestep with 2 small timesteps on which the acoustic waves were computed. The inner grid used a 2 s large timestep, again with three small timesteps per large timestep. Both grids had a 100 m vertical spacing in the lowest three kilometers and had a total of 83 vertical levels over a depth of 10

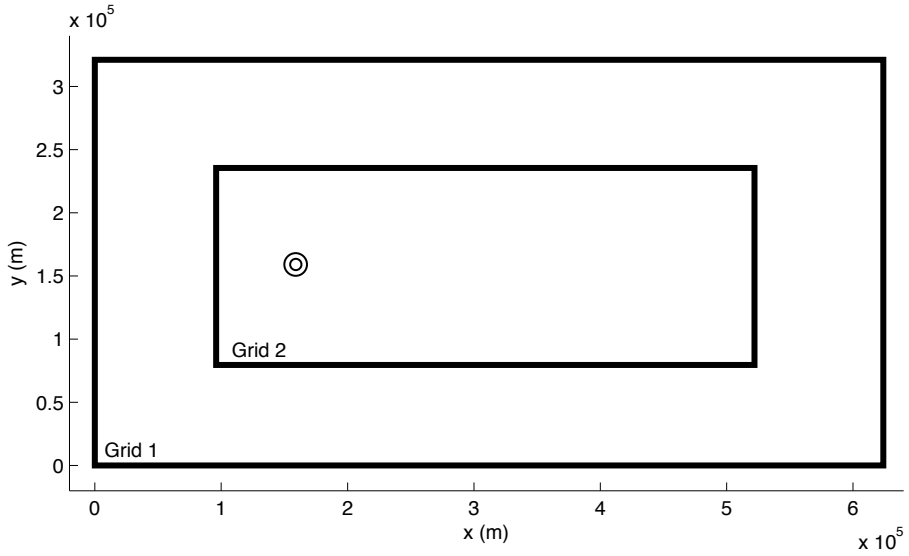

Figure 2.1: Grid geometry and mountain position for directional shear runs.

km. The outer grid is doubly periodic. A radiation upper boundary condition was used following Klemp and Durran (1983) and Bougeault (1983). A LeVeque advection scheme (LeVeque, 1996) was used for the advection of scalars to correctly handle the vertical gradients in potential temperature in these simulations. No Coriolis force is used ($f = 0$) to prevent the Coriolis force from biasing the wake, but a warm bubble was placed southwest of the mountain to start vortex shedding.

The directional shear runs are initialized with an idealization of the sounding taken from Sal, Cape Verde, on 2 June 2005 (Figure 1.4a). The Cape Verde Islands were chosen over other islands that commonly trigger vortex shedding, in particular Jan Mayen, Norway and Isla Guadalupe, Mexico, as Cape Verde has a station which regularly takes soundings (unlike Guadalupe) which are upstream of the islands seen to shed and not directly affected by the wake of a nearby mountain (unlike Jan Mayen). The thermal structure (Figure 2.2a) contained a 16.9 K inversion from 850 m to 1750 m corresponding to a buoyancy frequency N of 0.025 s^{-1}, a nearly neutral

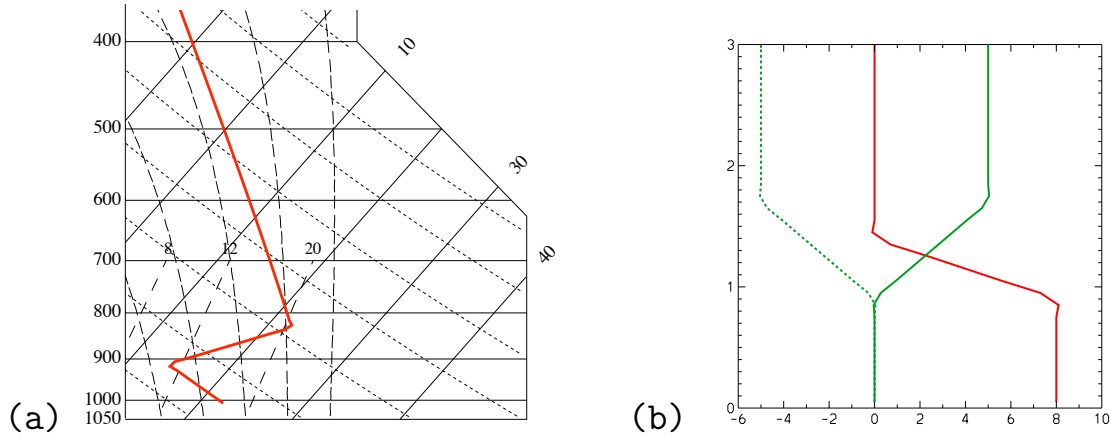

Figure 2.2: Directional shear initial condition profiles. (a)Temperature on a skew-T plot. (b) Wind profiles: u in red, v in solid green for the cyclonic simulation, dotted green for the anticyclonic simulation.

boundary layer below with $N = 0.00033$ s^{-1}, and constant $N = 0.013$ s^{-1} above.

Two different wind profiles were used (Figure 2.2b). Both have westerly 8 m s^{-1} winds throughout the boundary layer, but then turn through the inversion either to southerly to create a cyclonic turning of the wind or to northerly to create an anticyclonic wind profile. The shear is placed in the inversion to prevent dynamic instability from appearing. The u profile decreases linearly from 8 m s^{-1} at the bottom of the inversion to 0 at 1500 m, while v increases linearly from 0 at the inversion bottom to $\pm$ 5 m s^{-1} at its top depending on the specific simulation. Note that in the original sounding (Figure 1.4a) u decreases more rapidly than v does, which is recreated in the idealized sounding to represent this fact as well as to reduce the shear's magnitude to further avoid an undesirable Kelvin-Helmholtz instability.

The model runs were not initialized with the full wind profile, but instead started from rest; the profiles were then slowly increased over the next 1.5 hr to their full values, in order to avoid the creation of gravity waves due to an impulsive startup.

A round mountain is used in these simulations, with parameters $x_0 = y_0 = 159$

km, $\beta = 1$, and $a = 9$ km used in (2.1). The peak elevation H was 2 km, roughly the height of Santa Antão in the Cape Verde Islands.

2.4 Evolving Flow Runs

The evolving flow runs were performed with a lower resolution, triply nested grid to cover the same area as those by CDH and Chen et al. (2006) and to accommodate the synoptic square-wave flow used in some of the simulations. The grid geometry can be seen in Figure 2.3. The outermost grid used a horizontal resolution of 18 km, the second, 6 km, and the innermost, 2 km. The timesteps used were 18 s, 6 s, and 2 s, respectively, with only one small timestep. The outermost grid's dimensions were 1872 km by 1872 km; the second grid, 612 km by 612 km. The innermost grid's dimensions were dependent on the mountain used: for an elongated ridge the innermost grid measured 324 km by 324 km, while for the round mountain a more economical 324 km by 180 km grid was used. Doubly periodic lateral boundary conditions were again used in these simulations.

The vertical resolution was 150 m up to 10050 m, and then was stretched until the resolution became 500 m between 15000 m and the domain top at 28000 m. A total of 112 vertical levels were used. The evolving flow model runs did not use the radiation boundary condition, but instead applied a Rayleigh damper (as in CDH) in the upper 12 km of the model domain to absorb vertically propagating waves, thus requiring the larger number of vertical levels. The evolving runs all use a uniform $N = 0.01$ s^{-1}. Since the basic state is vertically uniform in all of the evolving flows, and as such strong vertical gradients in potential temperature are less likely, a computationally less expensive centered advection scheme was used instead of the LeVeque scheme. In addition, these runs did not use a warm bubble to start shedding, since vortex asymmetries were not being investigated, but instead a Coriolis force (with $f = 10^{-4}$ s^{-1}) was applied to cause vortex shedding.

Two types of evolving flow, both originally constructed by CDH, were used. The

(a)

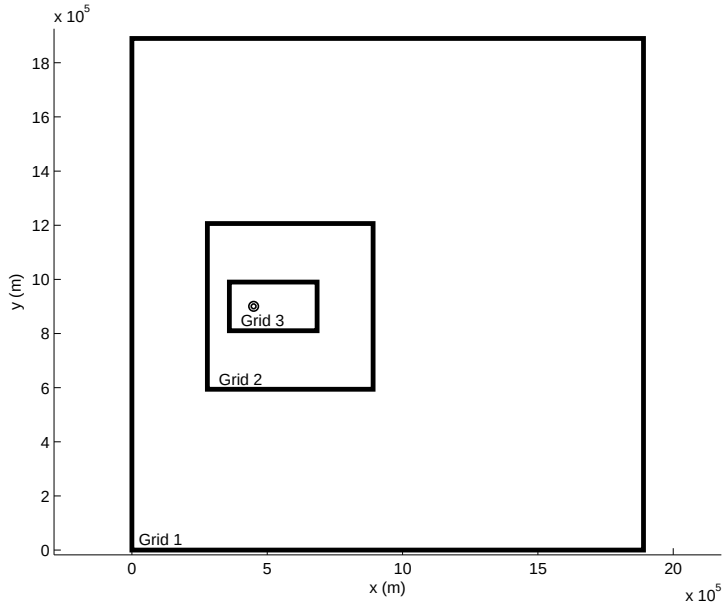

(b)

Figure 2.3: Grid geometry and mountain position for evolving flow runs. (a) Elongated ridge runs. (b) Round mountain runs.

first is an evolving uniform flow, which contains a spatially uniform time-varying westerly current:

$$U = U_0 \left(1 - \cos\left(\frac{2\pi t}{\tau}\right)\right)$$

where U_0 is 10 m s^{-1} and the flow evolution timescale τ is 50 hr in most cases. This flow begins at rest (and so removing the need for a gradual startup period), accelerates to 20 m s^{-1} at time 25 hr, and slows again to rest at time 50 hr. This flow is easily changed to longer timescales, such as 100 hr.

The second flow is a synoptic-scale square wave, a balanced large-scale flow which locally has the same time-dependent wind speed as the evolving uniform flow at the mountain, but varies spatially so that the flow is difluent during the accelerating phase and confluent during the decelerating phase, two features not present in the evolving spatially uniform flow. The initial square wave is given by

$$\begin{aligned} U &= U_0 \cos\left(\tfrac{2\pi(x-x_0)}{L_x}\right) \cos\left(\tfrac{2\pi(y-y_0)}{L_y}\right) \\ V &= U_0 \sin\left(\tfrac{2\pi(x-x_0)}{L_x}\right) \sin\left(\tfrac{2\pi(y-y_0)}{L_y}\right) \end{aligned} \tag{2.3}$$

where U_0 is again 10 m s^{-1}, $L_x = L_y = 1800$ km the dimensions of the domain, $x_0 = 450$ km, and $y_0 = 900$ km. This pattern is specified only at the outset, and the model does not maintain the pattern as the flow evolves; if the square wave is changed during the simulation, the model does not apply a forcing to recover the pattern. A constant, uniform 10 m s^{-1} westerly current is then superposed onto this square wave to propagate the pattern eastward and to create the time dependence. A depiction of this flow can be seen in Figure 2.4. Note how the flow in the vicinity of the mountain starts from rest, as in the evolving uniform flow, and then accelerates as the pattern moves to the east by the mean current.

To isolate the effects of flow evolution and the effects of flow confluence and difluence, or whether the effects seen here can be replicated in a steady, uniform flow, a series of model runs without any time evolution were performed. Three flows were used: steady uniform flow, where the basic state u is constant everywhere for all time;

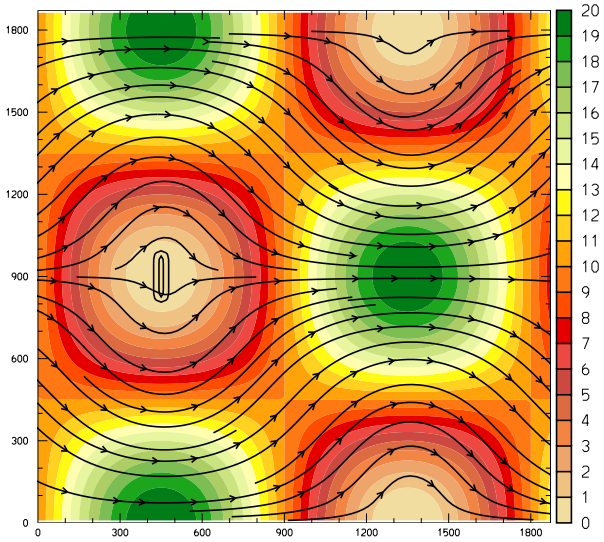

Figure 2.4: Initial position of the synoptic square wave. Color fill is u.

steady difluence, in which the square-wave of (2.3) is altered so difluence is present at the peak; and steady confluence. The steady difluence is reached by removing the constant, uniform westerly current, and shifting the wave so that $x_0 = 225$ km. The steady confluence is reached by the same process, except instead $x_0 = 670$ km. In both of these steady flows there are westerlies at the mountain peak's centerline of 10.6 m s^{-1}. These runs are started impulsively, with no gradual startup. The patterns in the steady difluent flow and the steady confluent flow are imposed at the outset of the simulation and are not maintained by the model afterward.

Two types of mountains were also used. The first is a 1.5 km high elongated ridge, with an aspect ratio β of 5. The other is a 3 km high round mountain, with $\beta = 1$. Both mountains are formulated by (2.1) and each has a half width a of 18 km.

A summary of the evolving flow and related steady model runs is given in Table 2.4.

Table 2.1: Evolving flow and related steady model runs.

Flow Type	Mountain Type	Flow Period τ
Evolving Spatially Uniform	1.5 km high ridge	50 hr
Evolving Spatially Uniform	3 km high round	50 hr
Evolving Square-wave	1.5 km high ridge	50 hr
Evolving Square-wave	3 km high round	50 hr
Evolving Spatially Uniform	1.5 km high ridge	100 hr
Evolving Spatially Uniform	3 km high round	100 hr
Steady Uniform 10 m s^{-1}	1.5 km high ridge	——
Steady Confluent	1.5 km high ridge	——
Steady Difluent	1.5 km high ridge	——
Steady Uniform 10 m s^{-1}	3 km high round	——
Steady Confluent	3 km high round	——
Steady Difluent	3 km high round	——

Chapter 3

DIRECTIONAL SHEAR AND VORTEX ASYMMETRY

3.1 Modeled asymmetry

The first goal of the simulations is to replicate the observed asymmetry in differing wind profiles seen in Figure 1.3 with the numerical model. Both of the directional shear runs show a clear asymmetry between the vortices of different signs in the developed wakes. In both cases the dominant vortices are those whose rotation has the same orientation as the turning of the ambient wind: cyclonic vortices dominate in cyclonic shear and anticyclonic vortices dominate in anticyclonic shear, reproducing the observed vortex asymmetry in Figure 1.3.

This asymmetry appears in several model fields and at multiple levels. The focus here is on the potential vorticity field, as it acts as a passive, conserved tracer in adiabatic, inviscid, non-dissipative flows, and so the strength of the vortices in terms of potential vorticity is ideally constant as they move downstream. In addition, potential vorticity encapsulates vorticity and potential temperature, both of which are important in creating the vortices seen in satellite images: the vorticity creates the circulation patterns seen in a vortex, while a positive potential temperature anomaly creates the clearing in a cloud layer indicative of a vortex. The asymmetry is clearly seen in the 600 m potential vorticity field seen in Figure 3.1. In this figure the vortices are well developed and axisymmetrized a short distance downstream of the mountain, but the cyclonic vortices in the cyclonic shear case (refer to Figure 2.2) depicted in Figure 3.1a appear much stronger in the potential vorticity field than do the anticyclonic vortices. By the same token, anticyclonic vortices dominate in the anticyclonic shear case (Figure 3.1b). Note that the two runs are nearly but not exactly mirror

images of one another.

Another anticyclonic shear simulation was performed with the bubble placed to the northwest of the mountain, instead of the southwest as in the two simulations above. This run, seen in Figure 3.1c, again has anticyclonic vortices which are much stronger than the cyclonic vortices. In fact, this simulation is very nearly the exact mirror image of the original cyclonic shear case (Figure 3.1a), which is to be expected as the initial conditions are mirror images of one another. Hence, the residual differences between the simulations in Figure 3.1a,b are due to the placement of the bubble. Runs have also been performed with a constant, vertically uniform wind speed of 8 m s^{-1}, no wind shear, and a warm bubble south of the mountain which result in no discernible asymmetry between the vortices (Figure 3.2).

This cyclonic-anticyclonic asymmetry is also found in the vertical vorticity (Figure 3.3a) and perturbation potential temperature fields (Figure 3.3b). The asymmetry in the vertical vorticity field is not as strong as in the potential vorticity field, but is still clearly present. The 800 m perturbation potential temperature field, which acts as a proxy for subsidence and thus clearing in a stratocumulus layer (and so is shown at a level nearer to the inversion than are the potential vorticity and vertical vorticity fields), show substantially warmer values in the cyclonic vortices than the anticyclones in the cyclonic shear run.

To quantify this asymmetry, the differences in the strengths between the two signs of vortices were computed for several fields. The 600 m potential vorticity at the center of each cyclone seen in Figure 3.1 is, from left to right, 10.1 PVU (potential vorticity unit, 10^{-6} K m^{-1} s^{-1}), 9.5 PVU, and 7.5 PVU. For the anticyclones, it is -3.1 PVU, -2.3 PVU, and -3.3 PVU. The value in the easternmost anticyclone is somewhat higher than the others; this may be a vestige of the startup process as it is the first vortex of either sign to have been shed. However, even the magnitude of potential vorticity in this vortex is substantially less than that of the weakest of the three cyclones, with a PV magnitude 64% less than the westernmost cyclone.

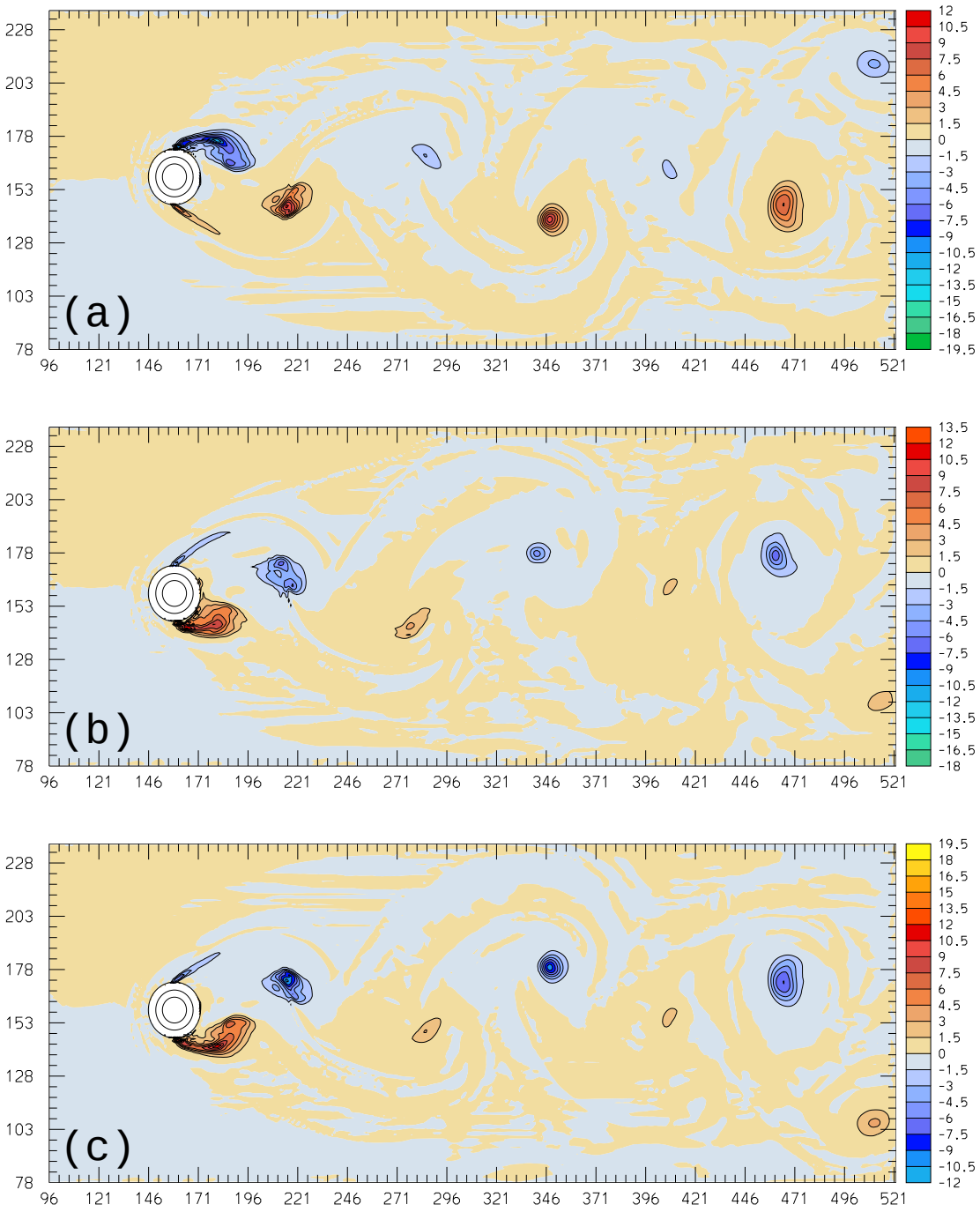

Figure 3.1: 600 m potential vorticity at time 18 hours. Contour interval is 1.5 PVU. Red colors indicate positive values, blue colors negative values. (a) Cyclonic shear simulation. (b) Anticyclonic shear simulation. (c) Anticyclonic shear simulation with the initial warm bubble moved to the north side of the mountain.

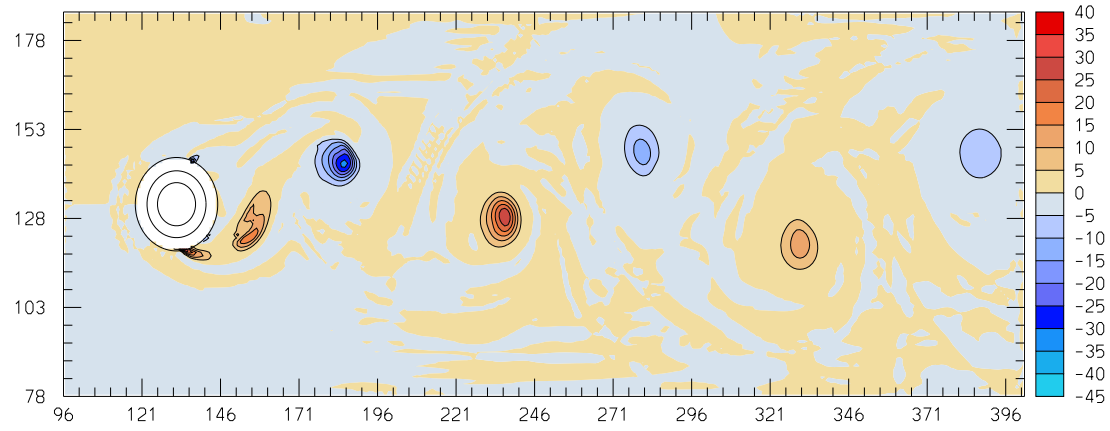

Figure 3.2: Same as Figure 3.1 except for a simulation with vertically uniform winds, a 5 PVU contour interval, and a smaller domain.

The 600 m vertical vorticity at the center of each cyclone is 0.0022 s^{-1}, 0.0018 s^{-1}, and 0.0013 s^{-1}, respectively, whereas for the anticyclones they are -0.0013 s^{-1}, -0.0011 s^{-1}, and -0.0011 s^{-1}, again from west to east. The strongest anticyclone has about the same magnitude as the weakest cyclone, but in each individual pair the cyclone is stronger, especially near the mountain where the anticyclone's ζ is only 60% of that of the accompanying cyclone. The 800 m theta perturbations are 3.3 K, 3.3 K, and 4.1K for the cyclones and 2.3 K, 1.3 K, and 1.9 K for the anticyclones. Note that the cyclone's theta anomalies become stronger as they move downstream, which may be compensating for the drop in vertical vorticity to conserve potential vorticity. The increasing potential temperature perturbation would also cause a more pronounced clearing in the vortex center, allowing the vortices to become more visible.

3.2 Tilting of basic state horizontal vorticity

The next goal is to quantify the process or processes that link the directional wind shear to the appearance of asymmetric vortex shedding. The hypothesis presented

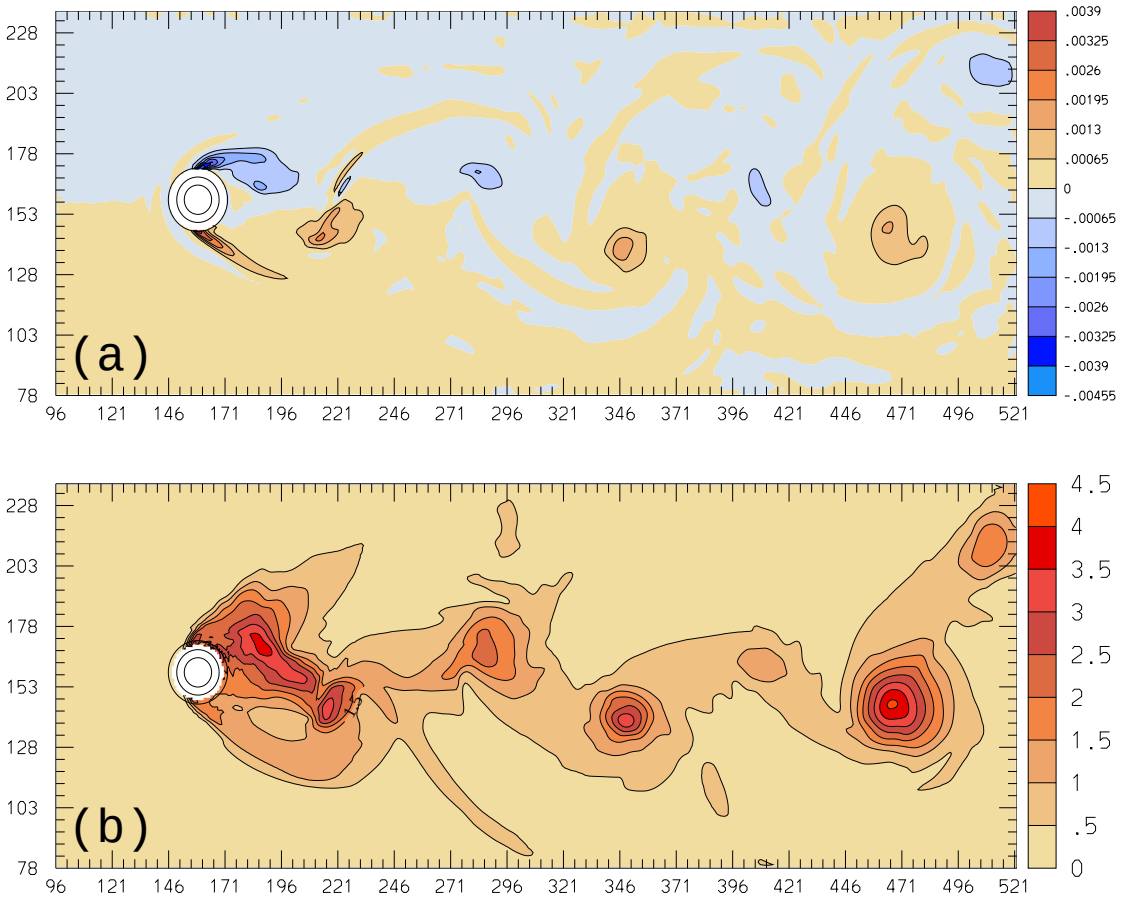

Figure 3.3: Cyclonic shear simulation fields at 18 hours. (a) 600 m vertical vorticity. Contour interval is 0.00065 s^{-1}. (b) 800 m potential temperature perturbation. Contour interval is 0.5 K.

here states that the basic state horizontal vorticity from the ambient shear is tilted into the vertical together with the baroclinically generated horizontal vorticity. This basic state vorticity is added to the baroclinically generated vorticity, causing an excess of one sign and a deficit of the other, which then would lead to a difference in the amount of vertical vorticity once the horizontal vorticity is tilted.

The first mechanism can be investigated by computing the patterns of the components of the vorticity vector $\mathbf{\Omega} = (\xi, \eta, \zeta) = \nabla \times \mathbf{u}$ and by diagnosing the various terms of the vorticity equation

$$\frac{\mathrm{D}\mathbf{\Omega}}{\mathrm{D}t} = (\mathbf{\Omega} \cdot \nabla)\,\mathbf{u} - \hat{\mathbf{k}} \times \nabla\theta, \tag{3.1}$$

in which the Boussinesq approximation has been applied to the baroclinic term, the last term on the right hand side (Holton, 2004, ch. 9). The cyclonic shear simulation will be analyzed here, although the same conclusions will be true for the anticyclonic simulations.

To begin, note that since the cyclonic shear produces a negative basic state $\frac{\partial u}{\partial z}$ and a positive $\frac{\partial v}{\partial z}$, while all other terms in the vorticity components are zero, the mean ξ and η in the shear layer are both negative. To show how this ties into the production of vorticity for the lee vortices, first recall that the mountain wave has potentially cooler air over the peak while there is potentially warmer air on the lateral sides of the mountain (Figure 1.2). From the baroclinic term in (3.1), which can be decomposed into $(\frac{\partial\theta}{\partial y}, -\frac{\partial\theta}{\partial x}, 0)$, it can be seen that the negative temperature gradient in the y direction on the south flank leads to the production of negative ξ, and on the north flank the positive temperature gradient causes the production of positive ξ. Thus, in the standard SR89 baroclinic production mechanism, there is negative perturbation ξ to the south and positive perturbation ξ to the north in a westerly current. The ξ from the basic state shear would then directly add to the baroclinically generated perturbation ξ, causing a greater magnitude thereof on one side; in the cyclonic shear case, on the south side. This added vorticity would then

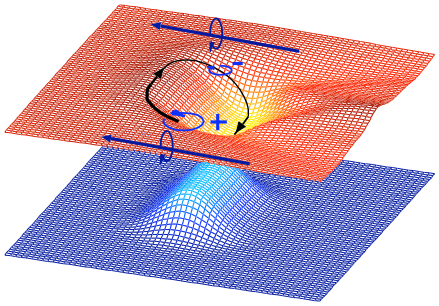

Figure 3.4: Modification of Figure 1.2 to show the effect of the basic state ξ on the SR89 vorticity generation process. Dark blue arrows represent the basic state ξ and the sense of rotation it imparts. Thickness of the vortex line (black) indicates the vortex line's strength.

be tilted to create a stronger vortex of one sign than the other; in the cyclonic shear case, the cyclonic vortex would be stronger. A schematic of this process can be seen in Figure 3.4, in which the basic state vorticity is added to the baroclinically generated vorticity present in the SR89 mechanism.

To support this line of reasoning, the relevant terms in the vorticity equation can be computed to determine whether the basic state shear vorticity directly contributes to the vortex asymmetry. Since vortex shedding implies the existence of an oscillatory wake, the fields presented in this analysis have been averaged over a shedding period (the length of time required for the wake to return to a given phase of the oscillation, or that over which one cyclone and one anticyclone are shed) to eliminate oscillatory effects in these variables. The length of a shedding period was determined to be about 6.33 hr once the wake settles into a quasi-steady state. The averaging interval used for the figures below is from simulation time 11.33 hr to time 17.33 hr, an interval 6.33 hr long when the starting and ending times are included. The averaged fields are not qualitatively different when slightly different intervals ($\pm$ 0.33 hr on either end) are used.

A $y - z$ cross section of the full ξ field is shown in Figure 3.5a. From this figure,

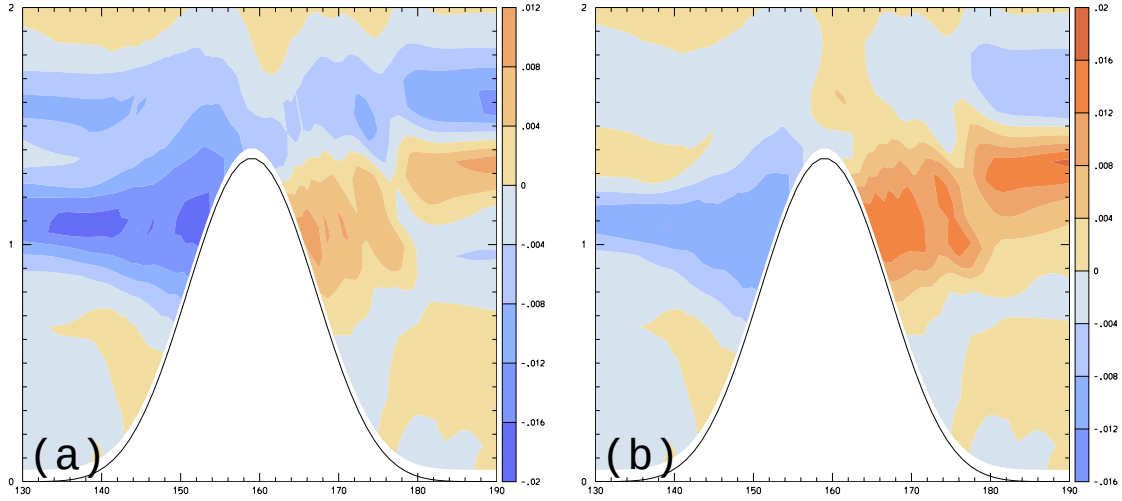

Figure 3.5: Time-averaged north-south cross-sections of ξ. Contour interval is 0.004 s^{-1}. South is at left. See Figure 3.6 for position of cross section. (a) Full ξ field. (b) Perturbation ξ field, with basic state vorticity subtracted.

it is clear that there is substantially more negative ξ on the south flank than positive ξ on the north flank. To demonstrate that this is the result of adding basic state vorticity and not additional baroclinic generation by the wave, the perturbation ξ field, $\frac{\partial w}{\partial y} - \frac{\partial (v - v_0)}{\partial z}$, is shown in Figure 3.5b. This figure shows that the magnitudes of perturbation ξ are nearly the same on both flanks, and actually slightly higher on the north flank. The conclusion is that the additional ξ seen in the simulation is due to the basic state shear and is not the result of a preference towards the baroclinic production of one sign of ξ in the mountain wave.

The next step in the SR89 process is the tilting of ξ into the vertical. The primary field of interest, the x-tilting term $\xi \frac{\partial w}{\partial x}$, is shown in Figure 3.6a. It is clear that the tilting is much greater on the south flank than on the north flank. The extremum on the south flank is 6×10^{-7}, whereas on the north flank it is only -3×10^{-7}. To show again that this is due to the added basic state vorticity, and not an enhanced w gradient, the field of $\frac{\partial w}{\partial x}$ is shown in Figure 3.6b. The magnitudes of $\frac{\partial w}{\partial x}$ are nearly

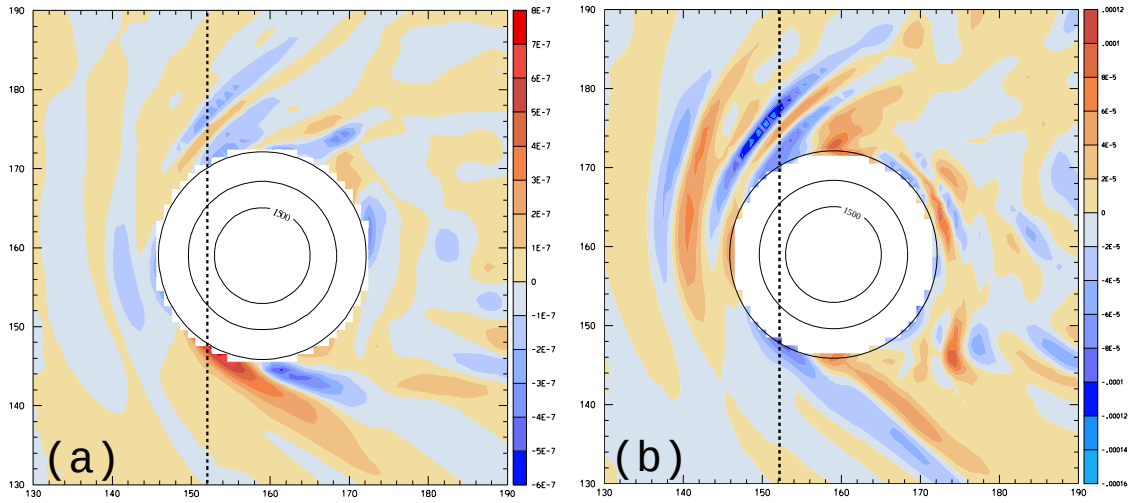

Figure 3.6: Tilting of x-component vorticity into the vertical. Dotted vertical lines indicate the position of the cross section depicted in Figure 3.5. (a) Time-averaged x-tilting $\xi \frac{\partial w}{\partial x}$ at 500 m. Contour interval is 10^{-7} s^{-2}. (b) Time-averaged $\frac{\partial w}{\partial x}$ at 500 m. Contour interval is $1.5{\times}10^{-5}$ s^{-1}.

the same on both sides, indicating that the greater tilting is not due to a stronger w gradient in the wave but because of the greater ξ present.

At this point it would be prudent to ask whether the basic state η may also cause an asymmetry through the same mechanism. By the same reasoning as above, it can be shown that there is not asymmetric tilting of η and that it cannot contribute to an asymmetry between the vortices. The term governing tilting of η into the vertical is $\frac{\partial w}{\partial y}\eta$. Basic state η is everywhere negative, but since w has a minimum over the peak $\frac{\partial w}{\partial y}$ is negative on the south flank and positive on the north flank. As a result, tilting gives positive ζ on the south flank and negative ζ on the north flank, in line with the signs of vertical vorticity which are usually generated in the SR89 process. Hence the basic state shear η cannot directly lead to asymmetric vortex shedding. This does not rule out the possibility of a stronger $\frac{\partial w}{\partial y}$ on one of the mountain's flanks due to the specific form of the sheared wave; this is left for further research.

It is now necessary to show that the vorticity generated by the SR89 process

along the flanks of the mountain does in fact become incorporated into the vortices downstream. This can be done by computing back trajectories from the vortices to determine whether the parcels in the vortices come from the tilting region. In addition, the computation of a trajectory can also provide a Lagrangian analysis of the evolution of the vertical vorticity and the potential vorticity for a given parcel, which is helpful in determining where these quantities are being generated and how they become incorporated into the vortices.

In this study, trajectories are computed "off-line" using the model's output, which is available at 5 minute intervals during the course of the simulation. A second-order Runge-Kutta integration scheme is used to calculate the parcel trajectories from the output. An off-line method allows for rapid computation of arbitrary trajectories after the simulation is completed and shows an air parcel's path to a reasonable degree of accuracy, but unlike the Lagrangian propagator analysis of ED02 this method has difficulty handling strong gradients and fronts and cannot take turbulent mixing into account.

Back trajectories from a cyclonic vortex with computations of vertical vorticity can be seen in Figure 3.7a. In this figure the trajectory clearly traces back from the cyclone and through the south flank of the mountain, where the tilting was observed to occur (Figure 3.6). In addition, this figure shows that a parcel following this trajectory gains a substantial amount of vertical vorticity in this tilting region, peaking at 0.0030 s^{-1}, although the amount of vorticity declines as it moves eastward. The vertical vorticity drops to a local minimum of 0.0008 s^{-1} as it passes south of the the starting point, but then gradually rises again to 0.0017 s^{-1} as it moves to the eastern edge of the figure.

It should be noted that both the trajectory itself and the vorticity along the trajectory are rather sensitive to the exact location of the starting point for the back trajectory. For example, a slightly different back trajectory does not pass directly through the tilting region, but instead originates in the wake's recirculation region

with very little vertical vorticity. It then gains vorticity as it turns around to head to the east as the first trajectory does. It is for this reason that the trajectories shown here originate not from the exact center of the vortices but from somewhat off of those centers. This sensitivity may indicate the need to compute the trajectories using finer time resolution data, or to compute a large ensemble of trajectories to examine the dispersion of parcels passing through a certain location.

The existence of different vorticity distributions along trajectories originating from nearby locations also suggests that there may be substantial entrainment of weakly rotational air into the vortices, which could explain the sudden decline in the amount of vertical vorticity on the parcel as it moves off of the mountain. This assertion is reinforced by plotting the subgrid-scale mixing field along the trajectory in Figure 3.8a. Here, a strong maximum in mixing can be seen at the region where the vorticity rapidly declines. However, despite the loss in vorticity in the lee, a large part of the vorticity gained through tilting along the trajectory is carried along the trajectory for its entire length.

Back trajectories emanating from the anticyclonic vortex are also computed in Figure 3.7b, which shows a parcel in the anticyclone which had passed through the north flank's tilting region at an earlier time. It picks up less vorticity in the tilting region than the cyclonic trajectory, corroborating with the Eulerian analysis of the tilting-related fields above, but undergoes less fluctuation in the amount of vorticity than does the cyclonic trajectory. The extremum value of vertical vorticity is only -0.0014 s^{-1}, but only declines to -0.0010 s^{-1} just before making a loop downstream. It shortly rises back to -0.0014 s^{-1} again before declining to only -0.0004 s^{-1} at the eastern end of the trajectory.

However, many of the back trajectories from the anticyclone are somewhat more complicated than those from the cyclone, and at later times trajectories become increasingly sensitive to the choice of starting point. This again may be a consequence of entrainment from the recirculation region, as seen from the strong sustained mix-

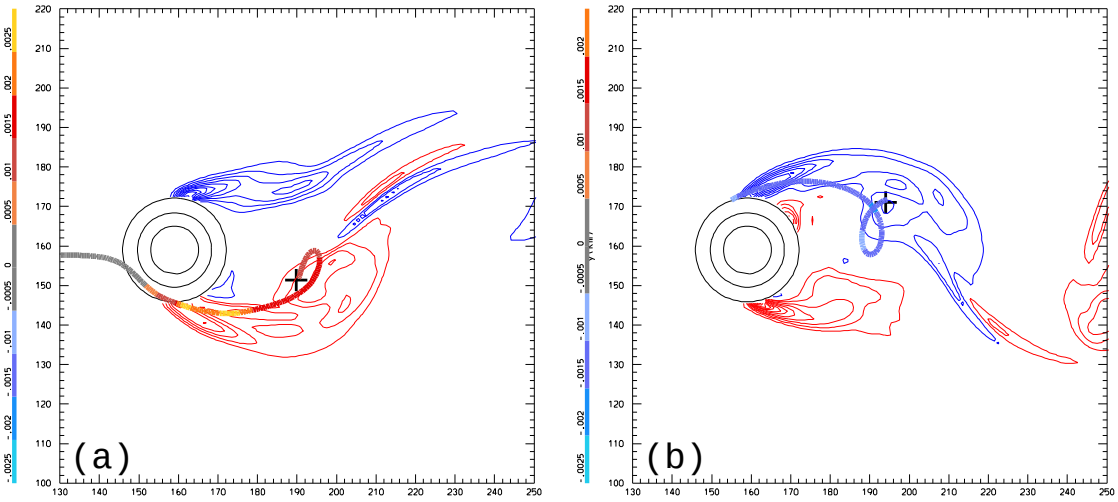

Figure 3.7: Vertical vorticity (contour interval: 0.0005 s^{-1}) with computed back trajectories beginning at the same time at 500 m. Color of trajectory indicates vertical vorticity. Cross represents the position of the trajectory's starting point. (a) Trajectory starting from cyclonic vortex at 16.5 hr with vertical vorticity field at time 16.5 hr. (b) Same as (a) but with a trajectory through the anticyclonic vortex at 13.5 hr and vertical vorticity field at time 13.5 hr.

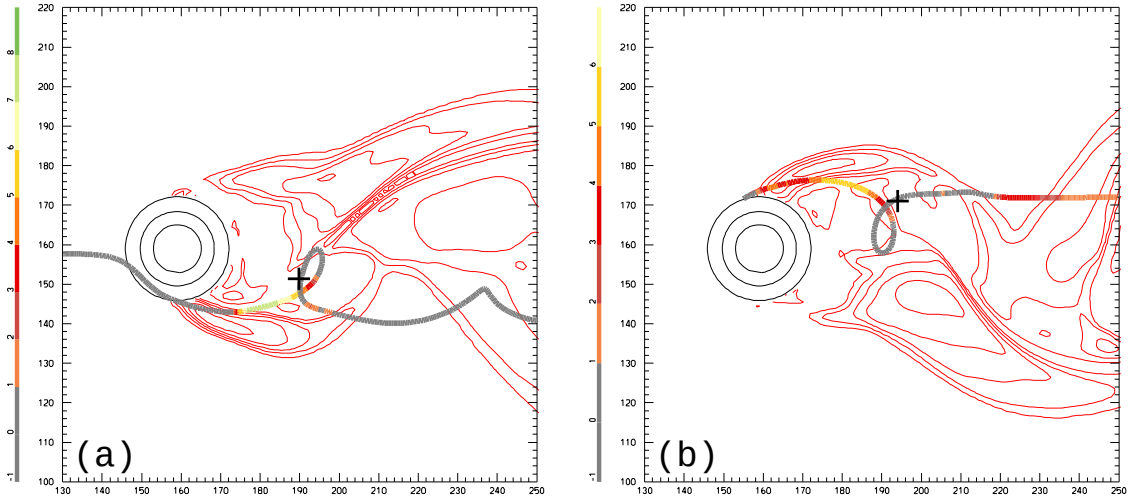

Figure 3.8: As in Figure 3.7, except with contours of subgrid-scale diffusivity (contour interval: 2 m^2 s^{-1}), color of trajectory indicates magnitude of mixing, and with forward trajectories computed as well.

ing along the trajectories in Figure 3.8b. The mixing is not as strong as for the cyclonic trajectory, but takes place over a wider length of the trajectory, entraining recirculating region mass from a wider area.

It is also instructive to compute the potential vorticity of a parcel following these trajectories, since in the absence of diabatic processes (in these simulations limited to thermal dissipation and mechanical and/or parameterized mixing) potential vorticity is conserved following the flow. The trajectory through the cyclone seen in Figure 3.7a is depicted in Figure 3.9a with potential vorticity along the trajectory's path computed. A parcel following this trajectory would gain a large amount of potential vorticity in the tilting region, peaking at 16 PVU, but drop to a minimum of 3.1 PVU as the parcel moves farther downstream. The parcel would then gain potential vorticity again farther down the wake, rising to 7.5 PVU east of the starting point and then experience only minor fluctuations as it moved eastward. The trajectory through

the anticyclone (Figure 3.9b) demonstrates a smaller drop in potential vorticity as it moves downstream, reaching its greatest amplitude at -7.5 PVU, changes between -4.6 and -7.6 PVU as it approaches the loop, and then declines to -2 PVU farther downstream.

A second proposed mechanism for the asymmetry is that the shear is modifying the form of the mountain wave such that the formation of the vortex of one sign is assisted or that of the other sign is hampered. This could stem from a number of specific mechanisms, such as the baroclinic generation of horizontal vorticity, the amount of tilting or stretching, or interference with wave structures above the shear layer. These effects could manifest themselves farther downstream as the fluctuations seen in vertical vorticity and potential vorticity seen above; in particular they could be the reason for the anticyclone's trajectory having greater values of both fields than the cyclone's trajectory for an interval along the trajectories. Another effect worthy of consideration is that of mixing in the lee, which could be the cause of the large drops in both vertical vorticity and potential vorticity seen along the trajectories as well as being a substantial source of potential vorticity downstream. These effects could be comparable in magnitude to that of the modified SR89 mechanism discussed above; work on these factors is slated for future research.

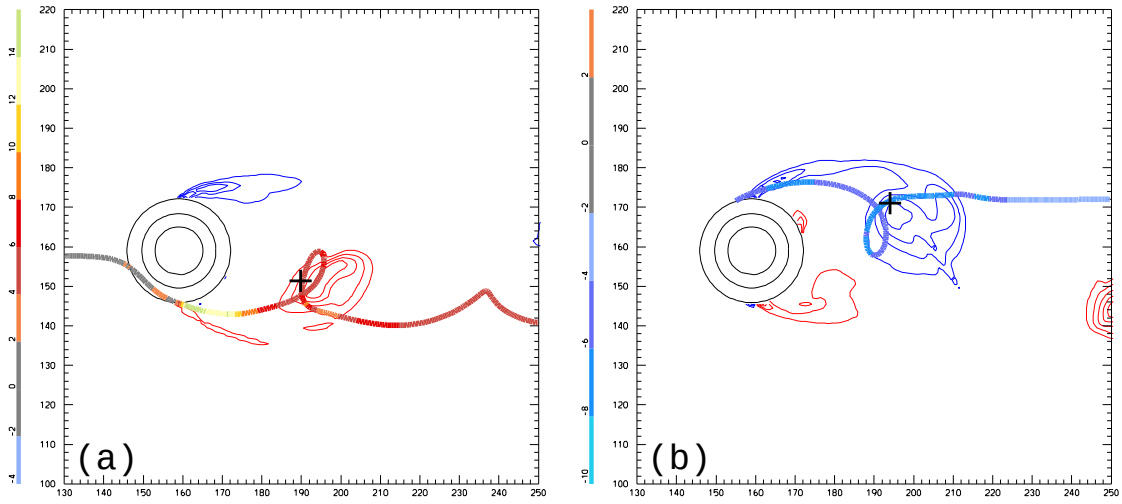

Figure 3.9: As in Figure 3.7, except with contours of potential vorticity (contour interval: 2 PVU), color of trajectory indicates magnitude of potential vorticity, and with forward trajectories computed as well.

Chapter 4

VORTEX SHEDDING IN AN EVOLVING FLOW

The primary goal of the research on evolving flows is to determine if vortices and the wake behave differently or have a different structure depending whether or not the flow is accelerating or decelerating. This work parallels that of CDH and Chen et al. (2006, henceforth CHD) to some degree in its investigation of pressure drag and the morphology of the wake, although on a smaller spatial scale and without the detailed focus on mountain waves and momentum fluxes in favor of the phenomenology of the modeled vortices. Also, in contrast with the material on asymmetric vortices presented in the previous section, this research is driven by theoretical considerations of how flow evolution alters the vortices rather than by observations of differing vortex behavior in different wind regimes. The focus will be on two situations: flows past a 1.5 km high elongated ridge and those past a 3 km high round mountain. The flows used in this chapter are discussed in detail in section 2.4. Note that no true vortex shedding appears in the wake of a 1.5 km high round mountain and vortex shedding from the 3 km high ridge is too complicated to permit a thorough analysis at this time.

4.1 Discussion of evolving flows

We start by describing the vortex and wake behavior for the 1.5 km high ridge. The discussion will focus on the structure of the vortices at the surface, where they are the most well-formed in these simulations with vertically uniform stratification. The synoptic square-wave flow past a 1.5 km high ridge is the same situation that CHD looked at in the analysis of large-scale effects in their sections 4 through 7, and some

of the features noted here are seen in CHD as well.

The evolution of the wake structure in the square-wave flow is shown in Figure 4.1. Notice in particular that despite the slow, two-day timescale of flow evolution, the wake looks very different in the accelerating phase (Figure 4.1a,b) than in the decelerating phase (Figure 4.1c,d) despite the values of ε being identical in (a) and (d) and in (b) and (c). In Figure 4.1a, the generation of vorticity is just beginning, whereas in Figure 4.1d two more intense vortices are seen directly up against the mountain. In Figure 4.1b, a pair of weak vortices can be seen tracking eastward and outward from one another separated by a strong hydraulic jump; alternately, in Figure 4.1c, a noisy wake is seen instead of the vortices depicted in Figure 4.1b. The structures in this wake later form the vortices seen in Figure 4.1d, as the Doppler shift pushes the wake up against the mountain and vortices take shape. These vortices are clearly larger, more intense, and better defined than those in the accelerating phase.

In the accelerating flow, the difluence pushes the vortices outward from the centerline, while the acceleration Doppler shifts the vortices and distends them in the direction of the flow; conversely, in the decelerating flow, the Doppler shift as well as the vortices' mutual propagation pushes the vortices back up against the mountain, while the confluence pushes them inward. Despite the asymmetry induced by the Coriolis force, periodic vortex shedding is not observed in either phase of this simulation.

The square-wave's wake can be compared to the evolving spatially uniform flow's wake in Figure 4.2, which imposes a strictly westerly current with no confluence or difluence throughout the simulation with the same variation in velocity in time at the peak as the square-wave. Here, the "evolving uniform flow" refers to a horizontally uniform evolving flow, distinct from the "steady uniform flow" discussed in the next section where the basic state wind is constant everywhere for all time. In the accelerating phase (Figure 4.2b) the same weak vortices and pronounced jump as in the square-wave's case can be seen. In the decelerating phase (Figure 4.2d) strong

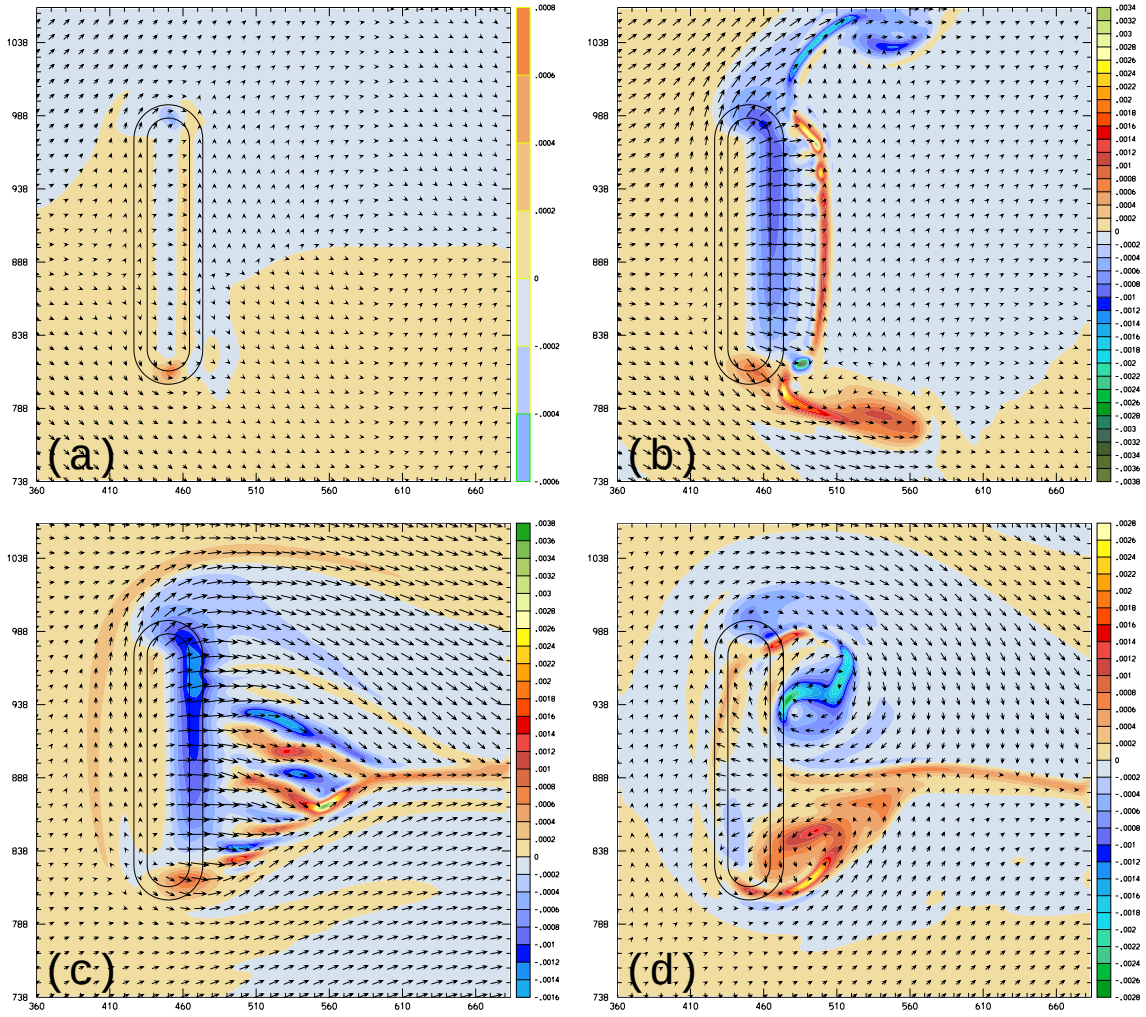

Figure 4.1: Surface vorticity and wind vectors, evolving square-wave, 1.5 km elongated ridge: a) 4 hr ($\varepsilon = 12$); b) 12 hr ($\varepsilon = 1.6$) ; c) 38 hr ($\varepsilon = 1.6$); d) 46 hr ($\varepsilon = 12$). The times depicted here are chosen for structural similarity between the flow phases, and not to strictly match ε.

vortices are again seen, but their mutual propagation in this case has pushed them farther apart. A strong hydraulic jump on the windward side appears due to the strong reversed flow between the vortices. In this case the decelerating-phase vortices are not as well formed as they are in the square-wave flow, but are larger and still better defined than in the accelerating phase of the same flow.

The lack of difluence in the accelerating phase creates little change in the vortex structure or behavior other than altering the path of the vortices, which do not substantially interact in either the square-wave or evolving uniform flows due to the distance between the two ends of the ridge. The vortex behavior is altered more greatly in the decelerating phase in the absence of confluence, since the vortices are not being pushed together by the uniform current and are instead forced apart by one another along the ridge. The broader reverse flow jet between the vortices in the decelerating phase of the uniform flow does allow a well-defined hydraulic jump to form.

A major difference between the accelerating and decelerating flow phases is the amount of wave breaking aloft in the lee of the mountain. In the accelerating phases of both the square-wave and evolving uniform simulations, relatively little flow reversal and isentrope overturning can be seen in the cross sections of Figures 4.3a and 4.3c, and as such there is little wave breaking. On the other hand, in the decelerating phase of both simulations, seen in Figures 4.3b,d, substantial regions of reversed flow and overturning can be seen, indicating a large amount of wave breaking. Both simulations have breaking starting at the beginning of the decelerating phase, occurring first at elevations of 2–4 km, and then at later times (around time 38 hr) appearing primarily between 1 and 2 km, and finally joining with the wake's reverse flow after time 40 hr. These results agree with those of Crook et al. (1990), with breaking appearing in a decelerating flow but not an accelerating flow, as does the pattern of breaking during the decelerating phase first occurring aloft and then descending to the surface.

A 100 hr timescale evolving uniform flow can also be analyzed to determine

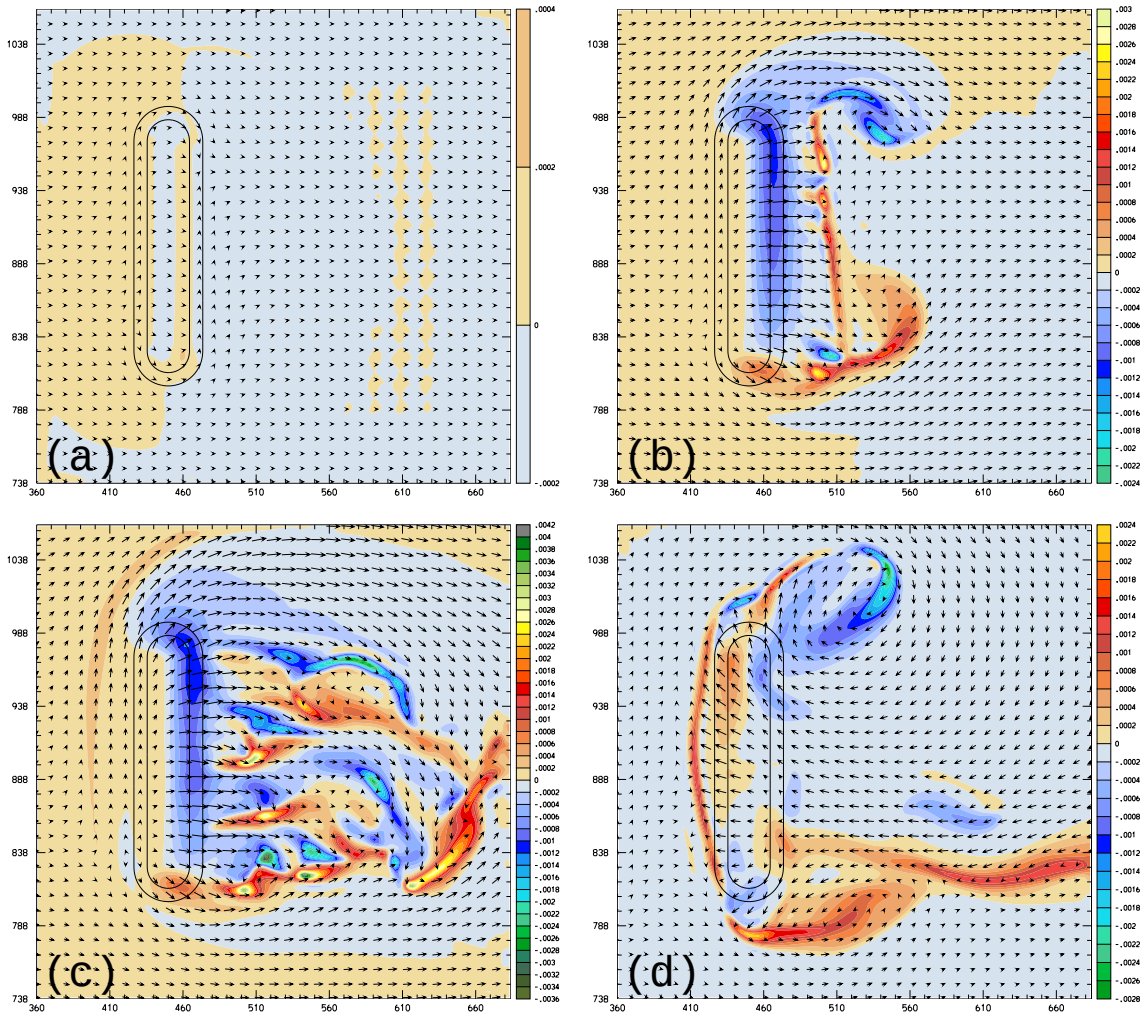

Figure 4.2: Same as Figure 4.1 but for the evolving uniform flow.

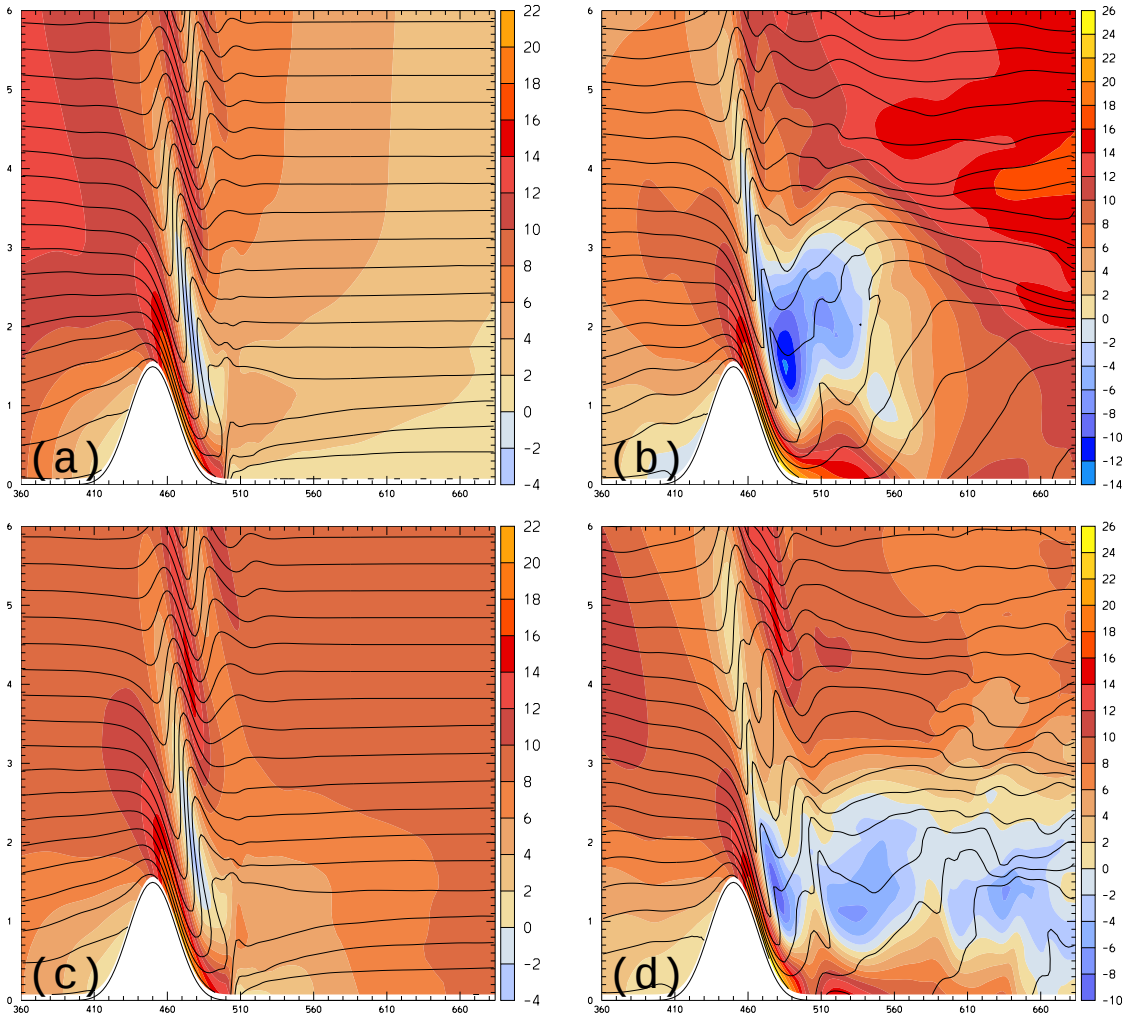

Figure 4.3: Cross-section in $x - z$ of u (color fill) and isentropes (black contours, contour interval 1 K) across the center line ($y = 900$ km), 1.5 km elongated ridge. In all panels $\varepsilon = 1.6$. a) Square-wave, 12 hr; b) square-wave, 38 hr; c) evolving uniform, 12 hr; d) evolving uniform, 38 hr.

whether a longer timescale can alter the behavior and structure of the vortices. The accelerating phase in Figure 4.4a shows the shed dipole again, as for the same value of ε seen in Figure 4.2b, although the vortices are better developed and larger, possibly the result of having more time to build vorticity before the higher speeds at later times advect the vortices downstream. Weak reverse flow is present here, which was not seen in the 50 hr timescale flow. In the decelerating phase, the vortices are seen to propagate downstream as a dipole between hours 75 and 80 before the reverse Doppler shift pushes the vortices back towards the mountain. The vortices are well formed and intense shortly after being shed (Figure 4.4b), but at later times become weaker and more diffuse (Figure 4.4c). Particularly notable here is that the vortex dipole seen in the accelerating (Figure 4.4a) and decelerating (Figure 4.4b) phases have the same structure, which was not seen in the shorter timescale simulations. In both the accelerating and decelerating phases, the longer timescale yields larger vortices. In the decelerating phase the tendency for deceleration to Doppler shift the vortices backward is reduced somewhat due to the slower flow decleration.

The 3 km high round mountain, by virtue of its greater height, causes a more nonlinear wake and will lead to differences in the formation, structure, and perhaps behavior of the vortices from that seen for the 1.5 km high ridge. The 3 km high mountain in the square-wave pattern creates a nearly symmetric vortex dipole (Figure 4.5a) with two well-defined, circular vortices in the accelerating phase. A few hours later (Figure 4.5b) the wake is seen to break up and shed for a short period before the flow becomes too fast (and so too linear) at later times to create vortices. These shed vortices are not as well defined and are highly elongated compared to the well-formed vortices seen earlier. During the decelerating phase, the wake changes little (Figure 4.5c) to until the Doppler shift pushes the wake backward and forms new vortices. However in this case the anticyclonic vortex is heavily distorted by the cyclonic vortex and the mountain, and ends up being stretched around the mountain and between the mountain and the cyclone (Figure 4.5d). The reverse flow jet between the vortices

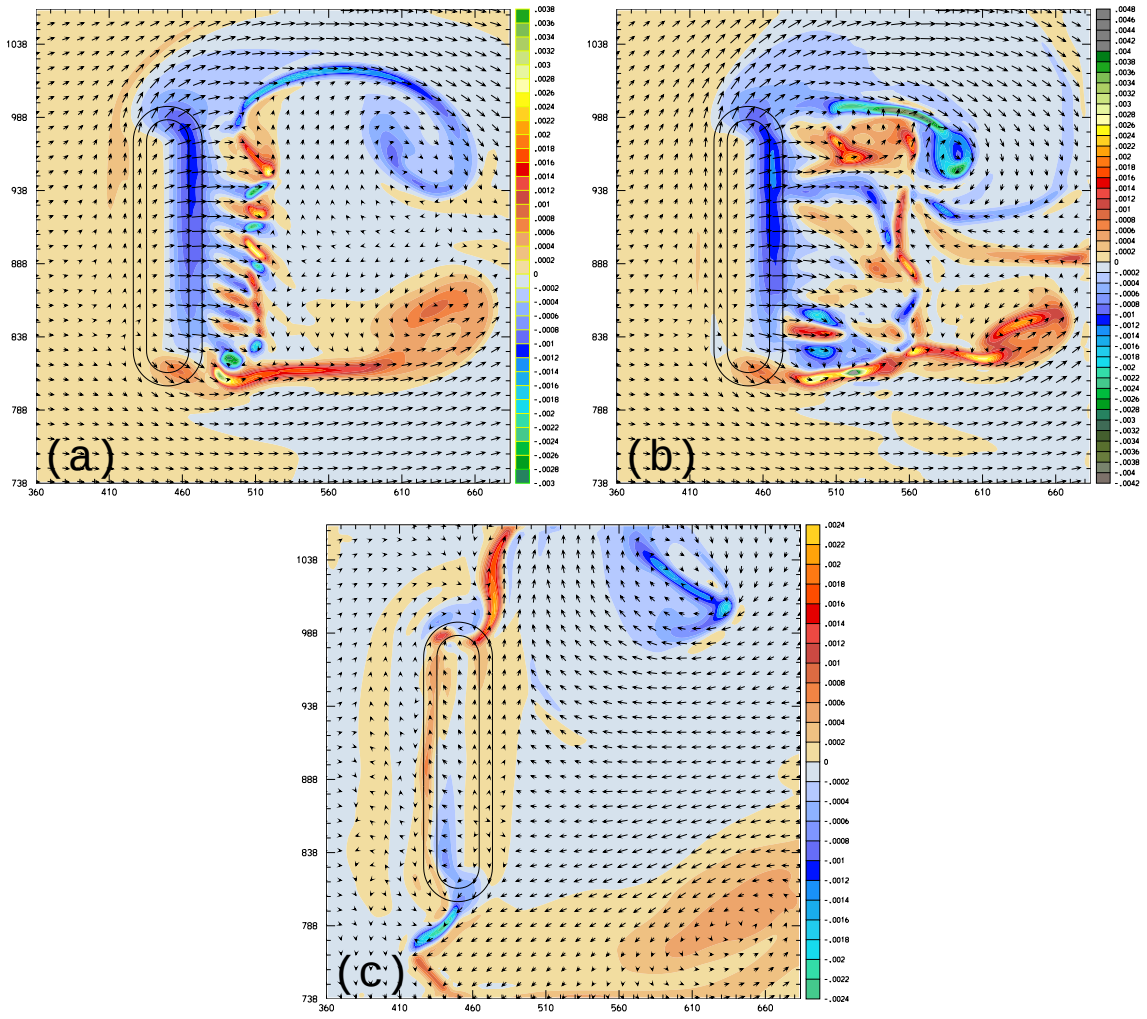

Figure 4.4: Surface vorticity and winds, 100 hr timescale evolving uniform flow, 1.5 km elongated ridge. a) 24 hr ($\varepsilon = 1.6$); b) 75 hr ($\varepsilon = 1.5$); c) 92 hr ($\varepsilon = 12$).

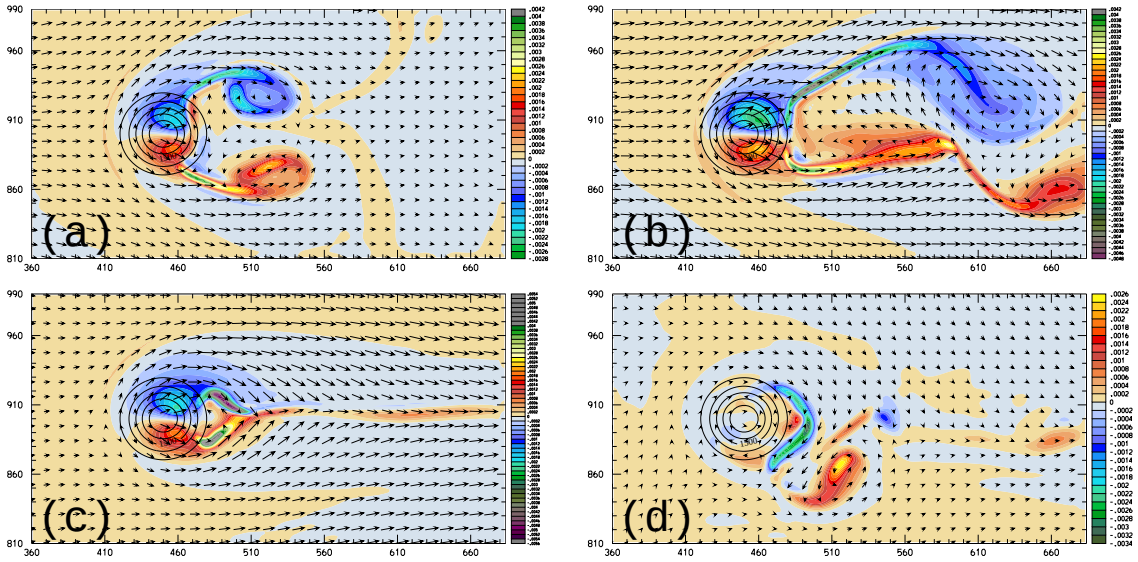

Figure 4.5: Surface vorticity and wind vectors, evolving square-wave, 3 km high round mountain. a) 14 hr ($\varepsilon = 2.5$); b) 20 hr ($\varepsilon = 1.7$); c) 36 hr ($\varepsilon = 2.5$); d) 46 hr ($\varepsilon = 24$).

does not flow up the mountain.

The evolution of the wake in the evolving uniform flow is similar to that for the square-wave, with a few notable differences. In the accelerating phase, shedding appears several hours earlier (Figure 4.6a) since there is no difluence pushing the vortices outward to prevent them from interacting as much. Also, during the decelerating phase the vortices are more symmetric and better formed (Figure 4.6d); in particular the anticyclone is better defined and is not as distorted, which is likely due to the lack of confluence pushing the anticyclone towards the cyclone. In this case, the symmetry of the vortices allows the reverse flow to impinge upon and be forced around the mountain. The decelerating phase vortices appear similar to those early in the accelerating phase of the square-wave flow (Figure 4.5a) in terms of shape and intensity; in both cases, no periodic shedding has taken place, so the vortices interact only weakly with one another.

The 100 hr timescale evolving uniform flow past a round mountain shows similar

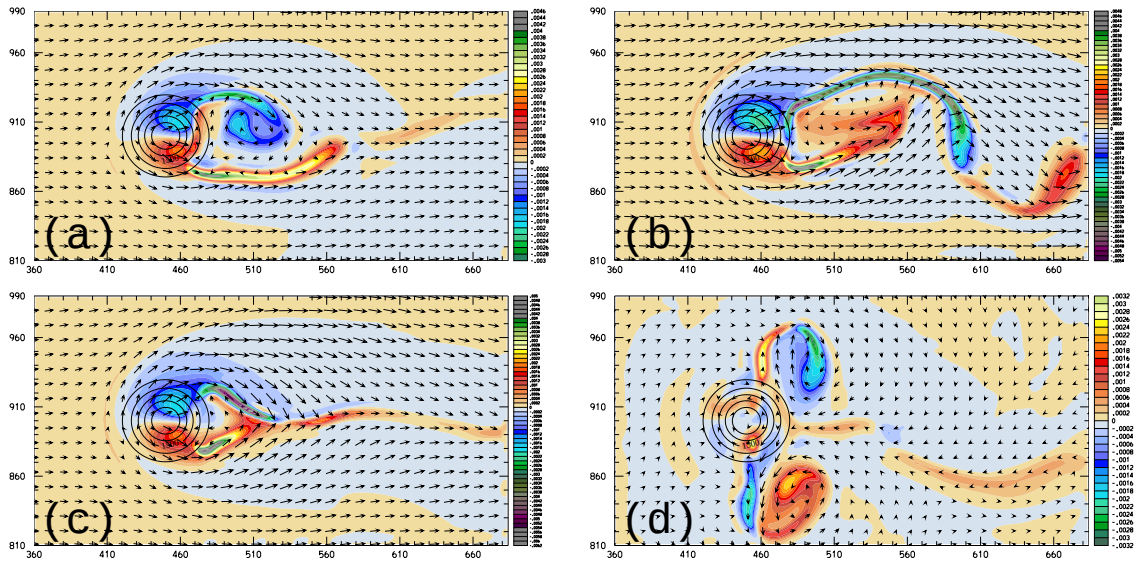

Figure 4.6: Same as Figure 4.5 but for the evolving uniform flow, and that figure (b) shows time 17 hr ($\varepsilon = 2.0$) instead.

behavior in its accelerating phase as the 50 hr timescale flow does. In Figure 4.7a vortex shedding can be seen, although with the slower timescale the vortices are somewhat better formed in this case. The decelerating phase does show substantial differences from its 50 hr counterpart. In particular, vortex shedding is seen for a short period of time in Figure 4.7b during the deceleration phase. As the backward Doppler shift continues later in the simulation the vortices stop propagating downstream, and the vortices then self-propagate to the northwest (Figure 4.7c), causing some distortion of the cyclonic vortex as well and a jet which does not flow up the mountain.

Wave breaking is not as strong over the 3 km high round mountain as it was for the 1.5 km high ridge, as can be seen by comparing the cross sections in Figure 4.8 to Figure 4.3. There is comparatively little breaking and little flow reversal aloft, as is to be expected for a round mountain compared to a ridge. Nearly all of the flow reversal is contained within the lowest 2 km above the surface and is attributable to recirculation in the wake instead of wave breaking. However, once again the strength

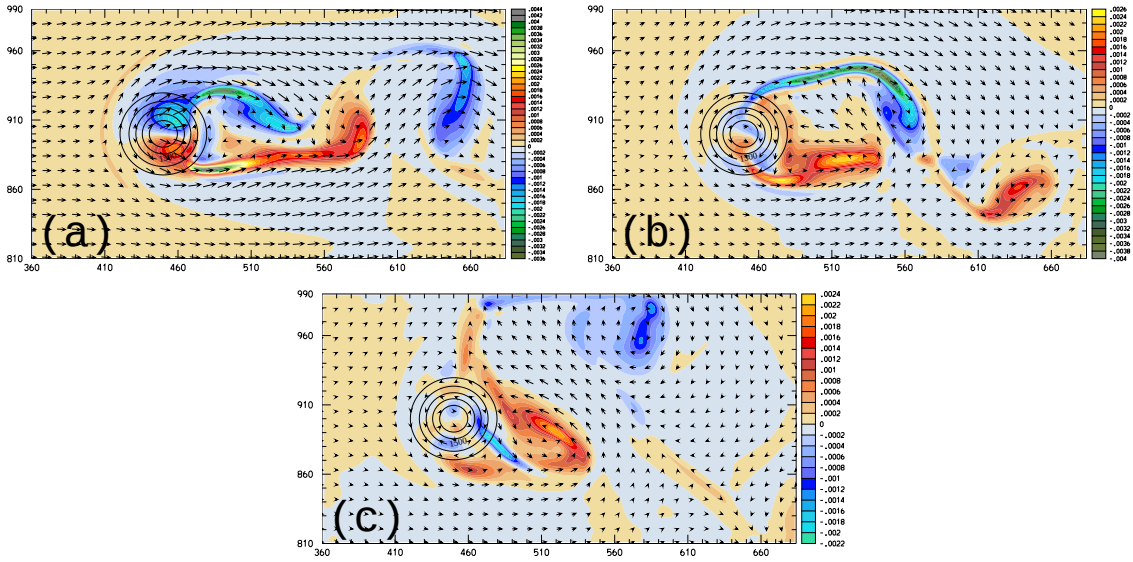

Figure 4.7: Surface vorticity and wind vectors, 100 hr timescale evolving uniform flow, 3 km high round mountain. a) 29 hr ($\varepsilon = 2.4$); b) 80 hr ($\varepsilon = 4.3$); c) 88 hr ($\varepsilon = 11$).

of the reverse flow in the accelerating phases (Figure 4.8a,c) is weaker than that in the decelerating phases (Figure 4.8b,d), which again could be associated with the Doppler shift in the flow clearing out the wake in the accelerating phase and pushing the wake up against the mountain in the decelerating phase.

From these simulations, three lee vortex behaviors have been seen. The first is the classical case of periodic vortex shedding, as in Figure 1.1, which was seen in the accelerating phases of both flows past the round 3 km high round mountain. Another is the shedding of a single vortex dipole, as in the accelerating phases of the flows past the 1.5 km high ridge and shortly in the decelerating phase of the 100 hr evolving uniform flow past the ridge. The last behavior is that of vortices that do not shed and remain in the lee, as seen in the decelerating phases of all of the 50 hr simulations above.

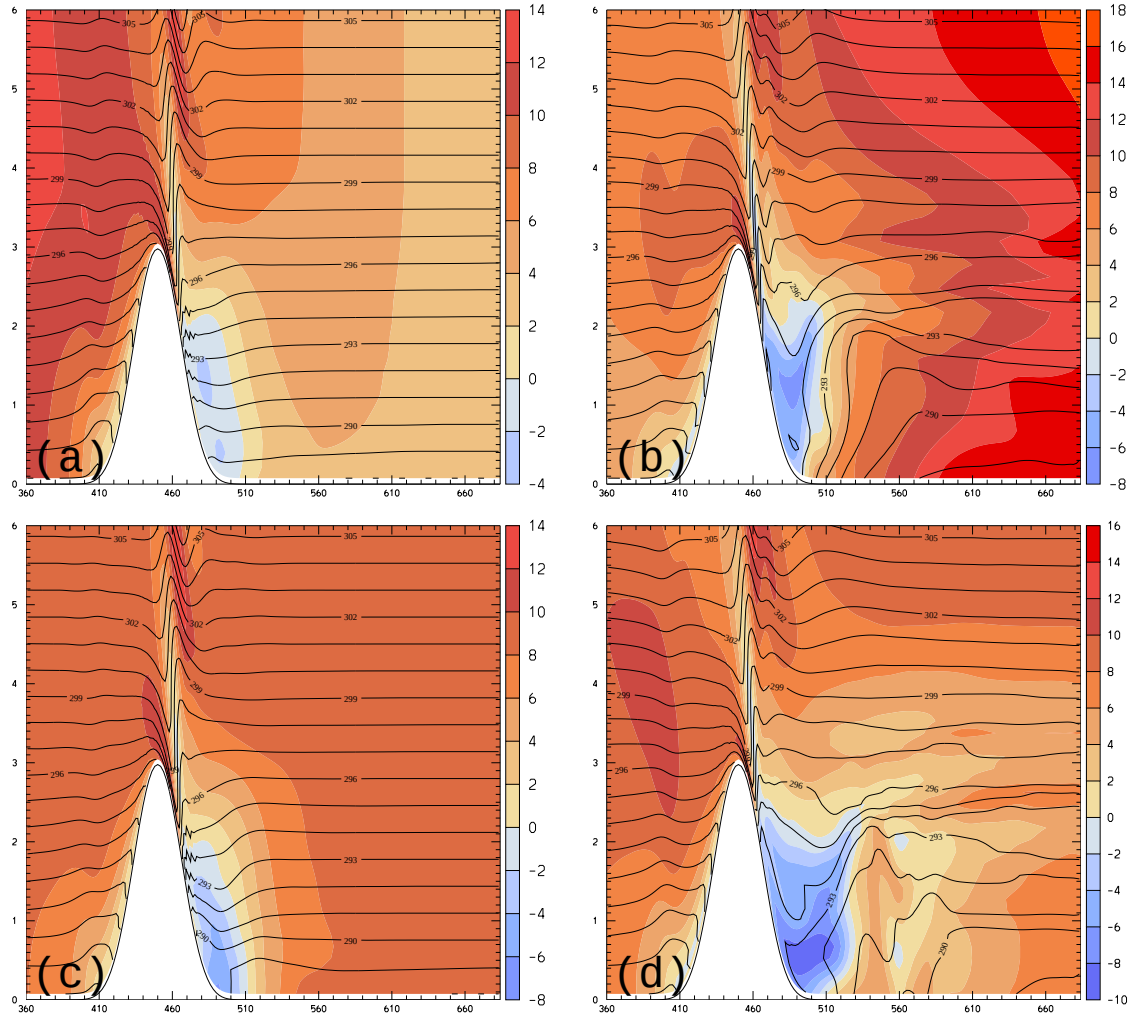

Figure 4.8: Same as Figure 4.3 except for the 3 km high round mountain. In all panels $\varepsilon = 3.2$.

4.2 Comparison to steady flows

To determine whether the vortex behaviors seen in the evolving simulations are due to the flow acceleration or deceleration, to flow confluence or difluence, or simply to the flow speed and thus purely ε, a number of steady flow simulations were performed, both with and without confluence or difluence. The steady and quasi-steady features seen in these simulations can be compared to the evolving flow simulations to determine the true influence of flow evolution on the lee vortices and the wake and to determine the conditions under which certain vortex behaviors take place. The values of ε in each of the steady, uniform simulations is 1.5 for the 1.5 km high ridge and 3 for the 3 km high round mountain; for the difluent and confluent flows, ε is 1.4 and 2.8, respectively, due to the slightly higher wind speed at the peak in the square wave. In this section, the times depicted in the figures below are chosen for structural similarity between the steady and evolving flows, and not to strictly match ε.

A comparison of the evolving and steady flows over the elongated ridge seen in Figure 4.9 show only minor differences in terms of wake structure and vortex behavior at the times depicted. In Figure 4.9a, the steady difluent flow shows similar but less well-formed vortices than in the accelerating phase of the square-wave flow (Figure 4.9b). The steady difluent flow shows two nearly steady vorticity filaments, one of each sign, extending from the ends of the vortices outward due to the difluence, although nothing which could be construed as vortex shedding beyond the initial vortex dipole which is shed. The wake is also substantially noisier in the steady difluent flow, due to the absence of forward Doppler shifting to clear out the wake and the lack of a shift towards lower ε and higher speed flow to produce less wake vorticity.

The steady confluent flow (Figure 4.9c) is also similar to the decelerating phase of the square-wave (Figure 4.9d) before the vortices appear. Both of the simulations show a triangular wake from the confluence and a shear line directed downstream. No vortices are seen in the steady confluent flow simulation.

These flows can further be compared with a steady, uniform $u_0 = 10$ m s^{-1} simulation. In this simulation a noisy wake can be seen (Figure 4.9e), although very slow periodic vortex shedding of large vortices with the scale of the ridge can be seen farther downstream when the larger 6 km grid is examined in Figure 4.9f. This behavior is not seen at any time in the other 1.5 km high ridge simulations, for either evolving flows or the steady confluent and difluent flows. Further simulations have shown that the vortex shedding period increases nearly linearly with the aspect ratio of the mountain, which is likely related to the increase in the advective timescale for more elongated topography.

The same comparisons can be made for the 3 km high round mountain. In Figure 4.10a a clear vortex dipole is seen in the steady difluent flow, in a similar fashion to that of the accelerating phase of the square-wave (Figure 4.10b). However, unlike in the evolving flow a period of vortex shedding is not seen in the steady difluent flow. The vorticity filament to the southeast of the mountain is seen to roll up into a vortex later in the simulation, although this may simply be the result of a barotropic instability. The confluent flows show very different results. The steady confluent flow (Figure 4.10c) is showing clear periodic vortex shedding, which is not present at any time in the decelerating phase of the square-wave (Figure 4.10d). The steady uniform 10 m s^{-1} flow (Figure 4.10e) shows periodic shedding similar to that in the steady confluence case.

From these simulations, three factors which decrease the likelihood of periodic vortex shedding have been identified, although none of these factors by themselves can prevent periodic shedding in all cases, nor can they always prevent dipole shedding and in some cases cause dipole shedding to appear instead of periodic shedding. An elongated ridge spreads apart the vortices which form on either end of the mountain, reducing the interaction between the two and preventing vortex shedding. In addition, the longer ridge has a longer shedding period and so needs the flow to remain in the shedding regime for a longer time interval for shedding to fully develop. The evolving

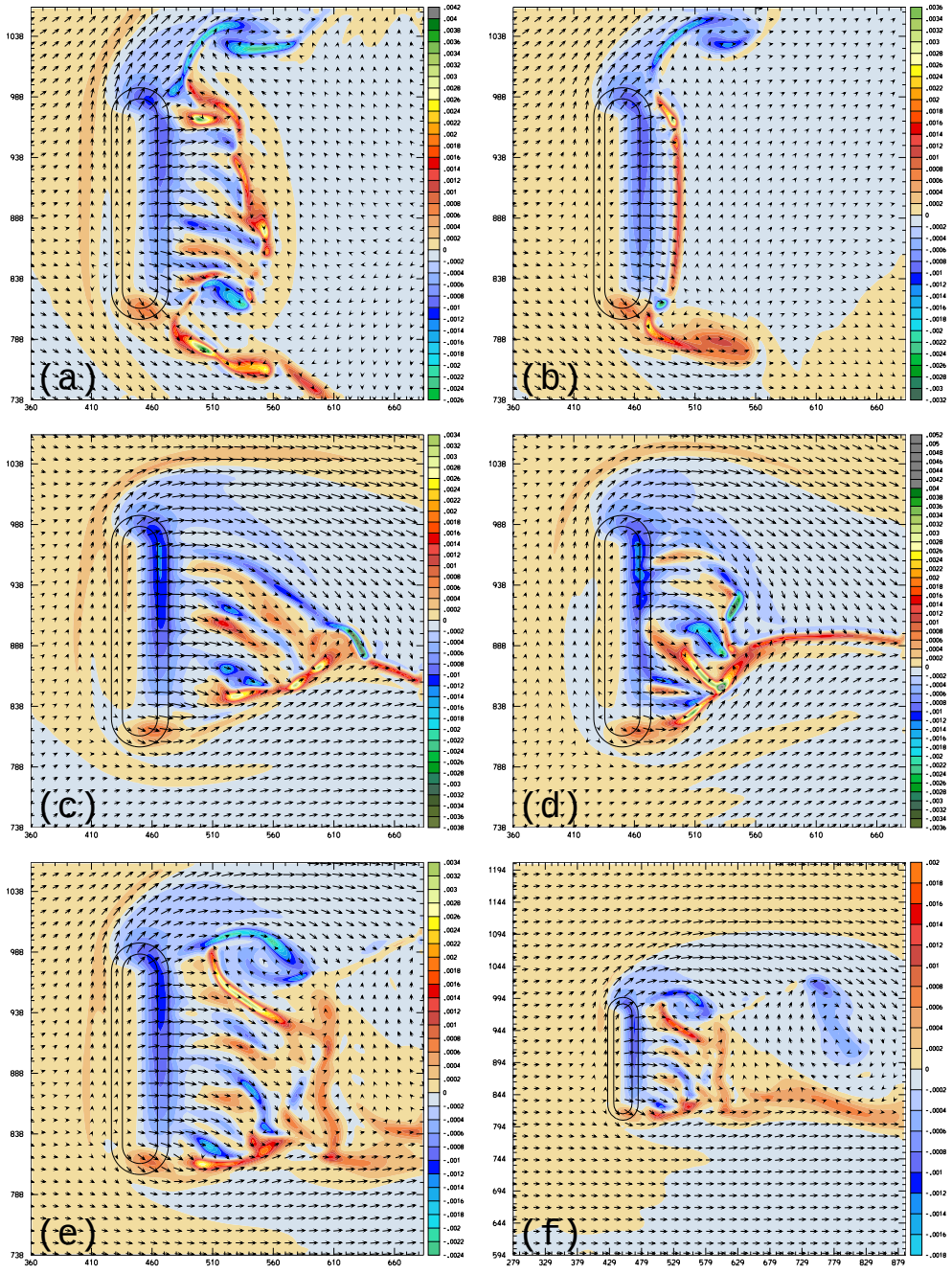

Figure 4.9: Surface vorticity and wind vectors, 1.5 km elongated mountain: a) Steady difluence, 7.5 hr ($\varepsilon = 1.4$); b) evolving square-wave, 11.5 hr ($\varepsilon = 1.7$); c) steady confluence, 20 hr ($\varepsilon = 1.4$); d) evolving square-wave, 40.5 hr ($\varepsilon = 2.4$); e) steady uniform, 25 hr ($\varepsilon = 1.5$); f) steady uniform on the 6 km grid, 25 hr ($\varepsilon = 1.5$).

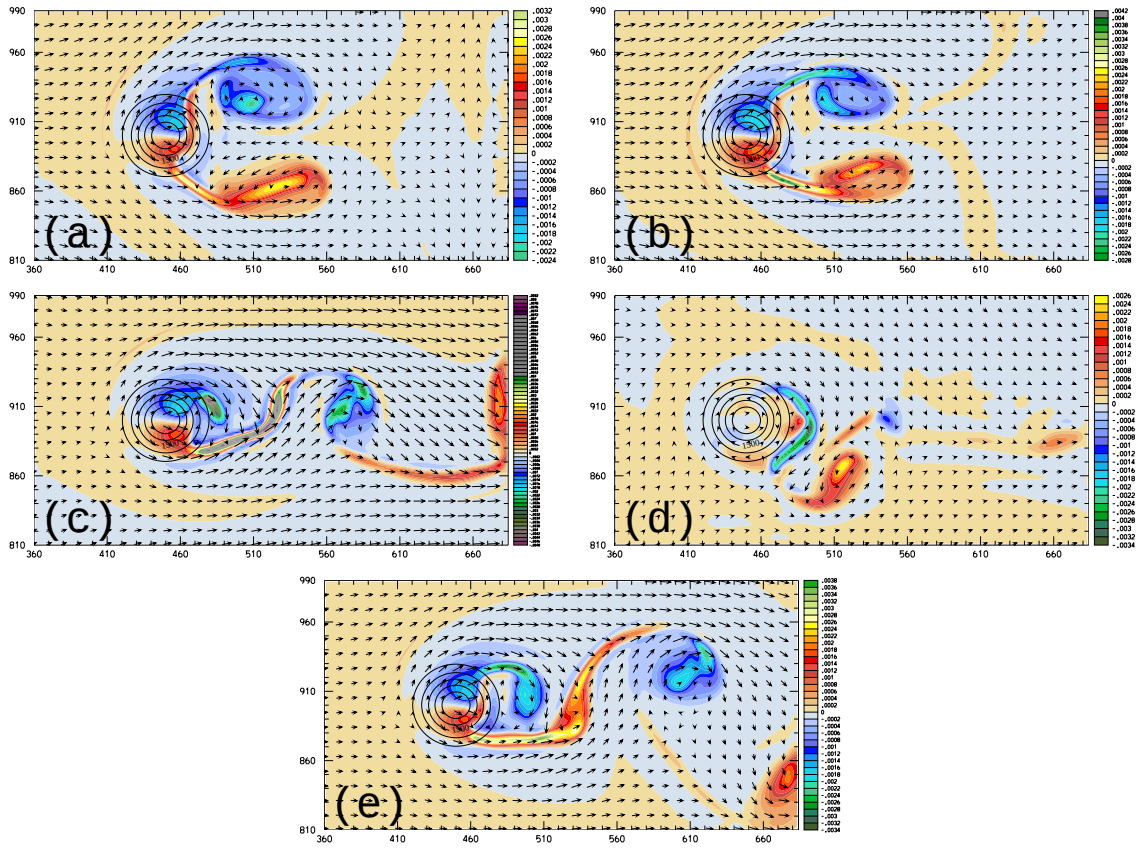

Figure 4.10: Surface vorticity and wind vectors, 3 km high round mountain: a) Steady difluence, 6.5 hr ($\varepsilon = 2.8$); b) evolving square-wave, 14.5 hr ($\varepsilon = 2.4$); c) steady confluence, 10.5 hr ($\varepsilon = 2.8$); d) evolving square-wave, 46 hr ($\varepsilon = 24$); e) steady uniform, 10.5 hr ($\varepsilon = 3$).

flows in particular move to regimes with flow too slow or linear to develop lee vortices. Periodic shedding is also less likely in difluent flows, where the vortices are again spread apart and do not interact as much. Both of these factors are often associated with dipole shedding instead of periodic shedding.

Flow deceleration is the third factor which reduces the probability of vortex shedding. Periodic shedding is seen in none of the 50 hr evolving simulations, as the backward Doppler shift pushes the wake and vortices back up against the topography and prevents their downstream propagation. The longer 100 hr timescale simulations have weaker deceleration and hence weaker Doppler shifting, and thus can allow periodic shedding for at least a short interval during the simulation.

Flow confluence is not seen to have a major effect on the vortices beyond pushing them inward towards one another and allowing greater interaction between the two vortices. This is particularly noticable in the heavy distortion of the anticyclone seen in Figure 4.5d. Periodic shedding is seen in the accelerating phase of the evolving flows past the 3 km high round mountain, but the vortices tend to be distorted into filaments as the acceleration shifts them downstream. Acceleration is not seen to discourage vortex shedding.

4.3 Pressure drag in evolving flows

A final aspect of the effect of evolving flows on lee vortices involves that on the surface pressure drag distribution of the mountain onto the flow. The effect of flow evolution and different mountains on the evolution of the pressure drag was also discussed by CDH and CHD. As in CDH, we examine the along-flow (east-west) component of the normalized pressure drag, defined as

$$D = \frac{1}{D_l} \int \int P \frac{\partial h}{\partial x} dA$$

where the integration is over the entire horizontal extent of the domain, $h = h(x, y)$ is the height of the topography, P is the surface pressure perturbation, and D_l the

steady state linear pressure drag. The linear, hydrostatic pressure drag is given by $\frac{\pi}{4}\rho_0 u_0 N(2a)(\beta+1)h^2$ for the ridge and $\frac{\pi}{4}\rho_0 u_0 N(2a)h^2$ for the round mountain, for east-west half width a, mean wind speed 20 m s^{-1}, and surface density ρ_0 taken as 1.2 kg m^{-3}. This value is taken from that for an infinite ridge with a Witch of Agnesi cross-section, and then multiplied by the cross-stream width of the localized mountain and range used here; for the round mountain the factor is just $2a$, and for the ridge it is $2(\beta+1)a$ to capture the length of the mountain and the flanks. The mountain used here, a $\cos^4(x)$ profile, will have a linear value differing only slightly from that of the Witch. The solution for the Witch, unlike that of the $\cos^4(x)$ profile, has a much simpler form that does not require the use of Fourier transforms to interpret, and so is used here.

The pressure drag for the evolving flows past the 1.5 km elongated ridge can be seen in Figure 4.11. In all three simulations there is an enhancement of drag by nonlinear effects. The flow demonstrates some degree of asymmetry between the accelerating and decelerating phases of the 50 hour evolving simulations. In particular, the evolving uniform flow demonstrates a substantial drop in pressure drag after the start of the decelerating phase, as well as reversed pressure drag in the final few hours of the simulation, likely due to the strong reverse flow between the vortices at this time. The square-wave shows weaker drag than the evolving uniform flow in the accelerating phase. When the evolving uniform flow is extended so the timescale is 100 hr, the resulting pressure drag is more symmetric between the accelerating and decelerating phases, with the exception of the sudden drop in drag at about 60 hr. These sudden changes are typical for mountains higher than about 500 m, as seen in CDH's Figure 10 and CHD's Figure 1.

Pressure drag for the 3 km high round mountain (Figure 4.12) is found to be less than that for the 1.5 km high ridge and less than linear theory would predict. This is expected as higher mountains are associated with greater blocking and flow around as well as the reverse flow due to strong lee vortices, all of which are nonlinear effects,

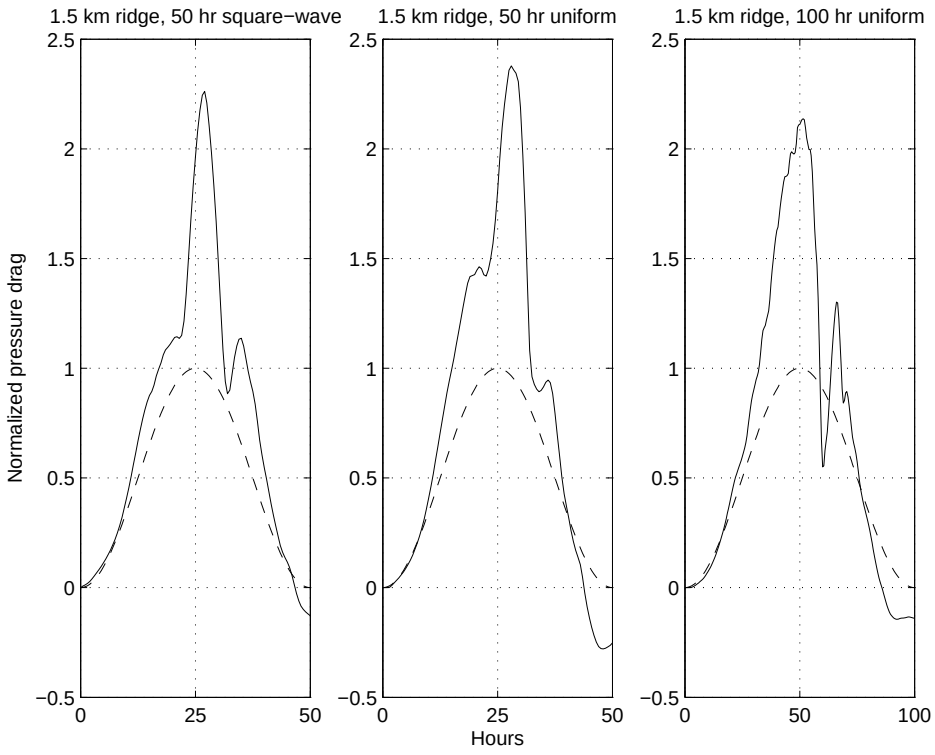

Figure 4.11: Pressure drag normalized with the linear hydrostatic pressure drag for a 20 m s^{-1} flow over a 1.5 km high ridge. Dashed line is the time-varying linear drag.

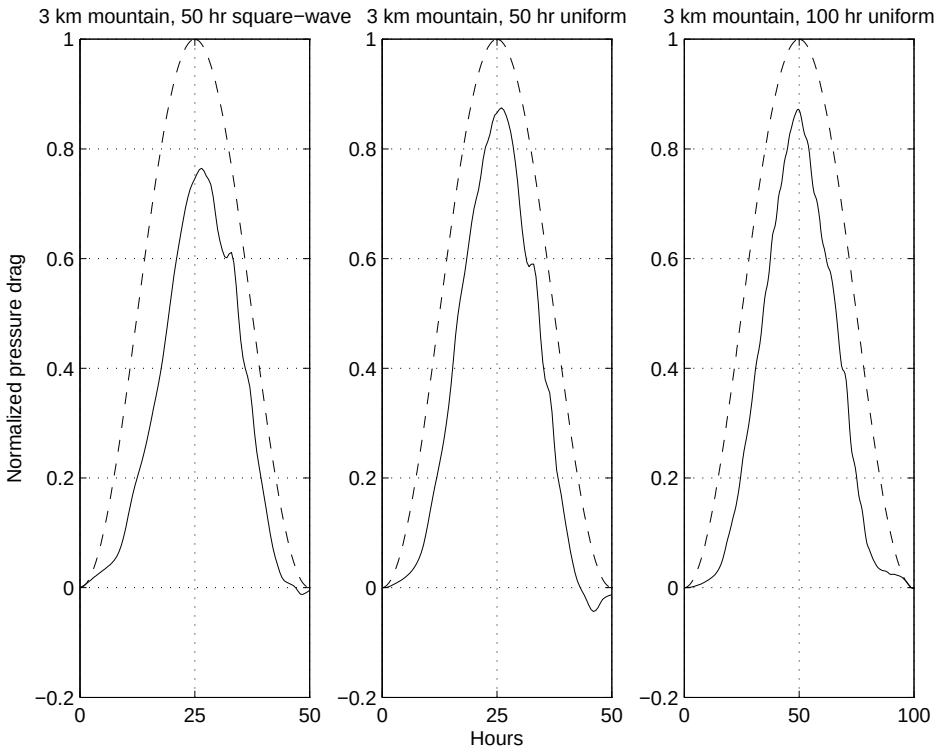

Figure 4.12: As in Figure 4.11 but for the 3 km high round mountain.

as has been found by several investigators (Schär and Durran, 1997; Bauer et al., 2000). The drag shows a fair degree of symmetry in time. The primary deviations from the symmetry are the "shoulder" between hours 30 and 35 in both simulations and the reversed pressure drag near the end of the evolving uniform simulation. This reversed drag is not as apparent in the evolving square-wave simulation since the jet of reversed flow between the deformed vortices does not flow over the mountain as it does in the uniform case. The 100 hr evolving uniform simulation depicts a strong symmetry across the midpoint of the simulation and lacks the shoulder and reversed drag seen in the other cases. Again, the lack of reversed drag results from the jet being directed away from the mountain, as seen in Figure 4.7.

Chapter 5

CONCLUSIONS

This research was carried out to investigate two issues regarding lee vortices. The first was to explain the appearance of asymmetric lee vortices during some observed vortex shedding events and to determine the environmental factors and dynamical processes responsible for the asymmetry. The second, an outgrowth of the research by Chen et al. (2005, 2006), was to determine the effect of flow evolution and the large-scale flow on the behavior and morphology of the vortices.

Numerical simulations motivated by observations of asymmetric vortex shedding show a clear asymmetry between the two signs of shed vortices in the presence of directional wind shear. The dominant vortex has the same sign as the sense of the turning of the wind with height: in cyclonic shear the cyclonic vortex dominates, and in anticyclonic shear the anticyclonic vortex dominates. This difference is clearest in the magnitude of the potential vorticity field, although it is apparent in the vertical vorticity and potential temperature fields as well. The asymmetry vanishes when the shear is replaced with vertically uniform winds.

It was proposed that the asymmetry arose from the tilting of the ambient vertical vorticity caused by the change in v with height due to the turning of the wind, in a simple extension of the Smolarkiewicz and Rotunno (1989) mechanism. To this end the relevant terms in the vorticity equation were computed and compared on each lateral flank of the mountain to see if any of the terms were greater on one side than the other. These fields were averaged over a full shedding period (during which one cyclone and one anticyclone is shed) to isolate the time-independent nature of the wake.

This analysis first found that the magnitude of the negative x-component vorticity ξ on the south flank of the mountain, where the cyclonic vortex forms, to be higher than the positive ξ on the north flank of the mountain, where the anticyclonic vortex forms. The next step, the magnitude of the x-tilting term $\xi\frac{\partial w}{\partial x}$, was also found to have a larger magnitude on the south flank than to the north. The asymmetries in these fields were also determined to be the result of the additional vorticity of one sign from the basic state, and not due to the particular form of the wave.

A trajectory analysis was then performed to determine whether the vertical vorticity ζ created through this process was later found in the shed vortices downstream. Back trajectories computed from the vortices downstream were found that had passed through the tilting regions on the mountain. Fields computed along these trajectories show the expected signs of vorticity and potential vorticity being generated and carried along. The trajectories show that both the vertical vorticity and potential vorticity start with larger values on the south side of the mountain in the tilting region; however, due to the strong mixing in the lee this vorticity is diluted somewhat as lower vorticity parcels are entrained into the cyclone, which is not seen in the anticyclone's trajectory. The trajectories then show the cyclone to have greater potential vorticity downstream. Due to the strong mixing in the lee and in the vortices themselves there was some uncertainty in following the back trajectories from the vortices to the tilting region on the mountain.

Two slowly evolving flows, a dynamically consistent synoptic-scale square-wave pattern and a uniform evolving westerly flow, were used to examine the effect of a non-steady flow and the particular form of that flow on the formation and structure of lee vortices. To determine which features were the result of the flow evolution and which were the result of the confluence and difluence in the square-wave or the instantaneous flow velocity, a series of simulations with steady flows with either confluence, difluence, or uniform westerlies over the mountain were performed.

As Chen et al. (2005) found, the character of the flow, including the form and

behavior of the vortices, could not be uniquely determined by the instantaneous value of ε, and the acceleration and deceleration of the flow must be considered as well. In particular, in all of the shorter timescale evolving flows, in the decelerating phase of the flow the vortices are forced by an upstream Doppler shift back up against the mountain, preventing any form of vortex shedding, whereas in the accelerating phase vortices are forced downstream and in some situations are observed to undergo periodic vortex shedding.

Three flow characteristics were found to inhibit periodic vortex shedding, as opposed to dipole vortex shedding or vortices which remain near the mountain and do not shed. As mentioned above, flow deceleration was seen to prevent vortices from shedding, which instead took the appearance of attached vortices. The other two factors, flow difluence and elongated mountain ridges, force vortices apart to prevent them from interacting and from starting the instability growth which leads to periodic vortex shedding. In these cases, a single vortex dipole is often seen to shed and move downstream instead of forming a continuous vortex street.

The amount of pressure drag was also computed to quantify some of the effects of flow evolution. The nonlinear enhancement seen in Chen et al. (2005) was found for all cases with the 1.5 km high ridge; however, the 3 km high mountain demonstrated no such enhancement, since the strong nonlinear effects at this height, blocking and flow diversion, reduce the drag on the flow. In addition, some degree of time asymmetry was found between the drag in the accelerating and decelerating phases of the flow. This asymmetry in time was more evident for flow over a 1.5 km high ridge than that over a 3 km high round mountain. In simulations with a 1.5 km high ridge, a number of sudden declines and rises in the amount of drag was seen, even when the timescale of flow evolution was doubled. Also, in a few simulations reverse pressure drag was observed in the decelerating phase when the reverse flow between the vortices impinged upon the mountain.

The work presented here on asymmetric vortex shedding has focused on the tilting

of basic state horizontal vorticity into the vertical as the cause of the vortex asymmetry. It is conceivable that the mountain wave could be altered by the directional shear in a manner which could alter the formation of the vortices, so that one sign of vortex would be preferred over the other. The analysis presented above shows that the wave is not causing a strong alteration of the primary tilting process, although other effects, such as the upper-level structure of the wave causing interference or structures from aloft coming down to the surface, could either promote or hinder the vortices. Strong mixing in the lee could also create or destroy vorticity and potential vorticity in the vortices depending on the particular structure of the mixing. The impact of these and other factors not directly related to the tilting of ambient vorticity is left for further research.

BIBLIOGRAPHY

Bauer, M., 1997: *Three-dimensional numerical simulations on the influence of the horizontal aspect ratio on flow over and around a meso-scale mountain*. Ph.D. thesis, University of Innsbruck.

Bauer, M., G. Mayr, I. Vergeiner, and H. Pichler, 2000: Strongly nonlinear flow over and around a three-dimensional mountain as a function of the horizontal aspect ratio. *J. Atmos. Sci.*, **57**, 3971–3991.

Bougeault, P., 1983: A nonreflective upper boundary condition for limited-height hydrostatic models. *Mon. Wea. Rev.*, **111**, 420–429.

Boyer, D. and X. Zhang, 1990: Motion of oscilliatory currents past isolated topography. *J. Phys. Ocn.*, **20**, 1425–1448.

Brighton, P., 1978: Strongly stratified flow past 3-dimensional obstacles. *Quarterly Journal of the Royal Meteorological Society*, **104**, 289–307.

Chen, C.-C., D. Durran, and G. Hakim, 2005: Mountain wave momentum flux in an evolving synoptic-scale flow. *J. Atmos. Sci.*, **62**, 3213–3231.

Chen, C.-C., G. Hakim, and D. Durran, 2006: Transient mountain waves and their interaction with large scales. *J. Atmos. Sci.*, **Submitted**.

Chopra, K. and L. Hubert, 1965: Mesoscale eddies in wakes of islands. *J. Atmos. Sci.*, **22**, 652–657.

Crook, N., T. Clark, and M. Moncrieff, 1990: The Denver Cyclone. Part I: Generation in low froude number flow. *J. Atmos. Sci.*, **47**, 2725–2742.

Durran, D. and J. Klemp, 1983: A compressible model for the simulation of moist mountain waves. *Mon. Wea. Rev.*.

Epifanio, C., 2003: Lee vortices. *Encyclopedia of the Atmospheric Sciences*, J. Holton, J. Pyle, and J. Curry, eds., Academic Press, 1150–1160.

Epifanio, C. and D. Durran, 2002a: Lee-vortex formation in free-slip stratified flow over ridges. Part I: Comparison of weakly nonlinear invicid theory and fully nonlinear viscous simulations. *J. Atmos. Sci.*, **59**, 1153–1165.

—— 2002b: Lee-vortex formation in free-slip stratified flow over ridges. Part II: Mechanisms of vorticity and pv production in nonlinear viscous wakes. *J. Atmos. Sci.*, **59**, 1166–1181.

Grubisić, V., R. Smith, and C. Schär, 1995: The effect of bottom friction on shallow-water flow past and isolated obstacle. *J. Atmos. Sci.*, **52**, 1985–2005.

Holton, J., 2004: *An Introduction to Dynamic Meteorlogy*. Elsevier Academic Press, fourth edition.

Hubert, L. and A. Krueger, 1962: Satellite pictures of mesoscale eddies. *Mon. Wea. Rev.*, **90**, 457–463.

Klemp, J. and D. Durran, 1983: An upper boundary condition permitting internal gravity wave radiation in numerical mesoscale models. *Mon. Wea. Rev.*, **111**, 430–444.

Kundu, P. and I. Cohen, 2002: *Fluid Mechanics*. Academic Press, second edition.

LeVeque, R., 1996: High-resolution conservative algorithms for advection in incompressible flow. *SIAM J. Numer. Anal.*, **33**, 627–665.

Lloyd, P., P. Stansby, and D. Chen, 2001: Wake formation around islands in oscillatory laminar shallow-water flows. Part 1: Experimental investigation. *J. Fluid Mech.*, **429**, 217–238.

Piani, C., D. Durran, M. Alexander, and J. Holton, 2000: A numerical study of three-dimensional gravity waves triggered by deep tropical convection and their role in the dynamics of the QBO. *J. Atmos. Sci.*, **57**, 3689–3702.

Potylitsin, P. and W. Peltier, 1998: Stratification effects on the stability of columnar vortices on the f-plane. *J. Fluid Mech.*, **355**, 45–79.

Reinecke, P. and D. Durran, 2006: Topographic blocking in flows with non-uniform upstream static-stability profiles. *J. Atmos. Sci.*, **Submitted**.

Schär, C. and D. Durran, 1997: Vortex formation and vortex shedding in continuously stratified flows past isolated topography. *J. Atmos. Sci.*, **54**, 534–554.

Schär, C. and R. Smith, 1993: Shallow-water flow past isolated topography. Part II: Transition to vortex shedding. *J. Atmos. Sci.*, **50**, 1401–1412.

Smith, R., 1989a: Comment on "Low froude number flow past three-dimensional obstacles. Part I: Baroclinically generated lee vortices". *J. Atmos. Sci.*, **46**, 3611–3613.

—— 1989b: Mountain-induced stagnation points in hydrostatic flow. *Tellus*, **41A**, 270–274.

Smith, R. and S. Grønås, 1993: Stagnation points and bifurcation in 3-d mountain airflow. *Tellus*, **45A**, 28–43.

Smolarkiewicz, P. and R. Rotunno, 1989: Low froude number flow past three-dimensional obstacles. Part I: Baroclinically generated lee vortices. *J. Atmos. Sci.*, **46**, 1154–1164.

Stansby, P. and P. Lloyd, 2001: Wake formation around islands in oscillatory laminar shallow-water flows. Part 2: Three-dimensional boundary-layer modelling. *J. Fluid Mech.*, **429**, 239–254.

Sun, W.-Y. and J.-D. Chern, 1994: Numerical experiments of vortices in the wakes of large idealized mountains. *J. Atmos. Sci.*, **51**, 191–209.

Zängl, G., 2005: Why is Alpine south foehn not associated with the formation of lee vortices? *Meteorol. Z.*, **14**, doi:10.1127/0941–2948.

Zhang, X. and D. Boyer, 1993: Laboratory study of rotating, stratified, oscilliatory flow over a seamount. *J. Phys. Ocn.*, **23**, 1122–1141.